Escola de Camins
Escola Tècnica Superior d'Enginyeria de Camins, Canals i Ports
UPC BARCELONATECH

PROJECTE O TESINA D'ESPECIALITAT

Títol

Validation study of a new implementation of the Discrete Element Method for an open source multiphysics code

Autor/a

Ignasi de Pouplana Sardà

Tutor/a

Eugenio Oñate Ibáñez de Navarra

Miguel Ángel Celigueta Jordana

Departament

737 - Resistència de Materials i Estructures a l'Enginyeria (RMEE)

Intensificació

Anàlisi i Projectes d'Estructures

Data

Juliol de 2013

Acknowledgments

I would like to especially thank Professor Eugenio Oñate for the opportunity to collaborate in the research performed in CIMNE (Barcelona). I have learned many concepts on the matter but what keeps in my mind as invaluable is the experience achieved during this time.

I also want to thank Miguel Angel Celigueta and Miquel Santasusana for the help and supervision received during the elaboration of this thesis.

Finally, I do not want to forget all the support that my family has always given me.

Title: Validation study of a new implementation of the discrete element method for an open source multiphysics code

Author: Ignasi de Pouplana Sardà

Supervisors: Eugenio Oñate Ibáñez de Navarra, Miguel Ángel Celigueta Jordana

Key words: Discrete Element Method (DEM), Linear-spring-dashpot model, Increment of energy, Discontinuum, Continuum, KRATOS, CIMNE.

Abstract

The Discrete Element Method (DEM) is a numerical technique that discretizes a material to simulate discontinuum or continuum through the interaction of large amounts of rigid elements.

The DEM Application is a C++ code of the Discrete Element Method that is being developed inside KRATOS, an Open-Source framework for the implementation of numerical methods for the solution of engineering problems.

Many different contact models have been applied in DEM simulations, but in the DEM Application we have been using the linear-spring-dashpot model. The linear spring generates the attraction or repulsive forces between the particles, and the dashpot represents a contact damping force that acts with the opposite sign of the velocity to dissipate energy. Without it, any system would be gaining energy at every time step because of the errors of the explicit time integration scheme and thus the results would have no validity.

The Discrete Element Method has proven to be a powerful and versatile numerical tool for modelling the behaviour of granular and particulate systems, and also for studying the micromechanics of materials such as soil at the particle level. However, the method also has the potential to be an effective tool to model continuum problems, especially those that are characterized by a transformation from a continuum to a discontinuum.

In this work, various experiments are performed with the aim of validating the code and verifying the current possibilities of the DEM Application. These analyses include: some tests of viscous damping, a sand clock model as a discontinuum example, and some continuum simulations with concrete test tubes.

Títol: Estudi de validació d'una nova implementació del mètode dels elements discrets per un codi obert multifísic.

Autor: Ignasi de Pouplana Sardà

Tutors: Eugenio Oñate Ibáñez de Navarra, Miguel Ángel Celigueta Jordana

Paraules clau: Mètode dels Elements Discrets (MED), model de molla lineal amb amortidor, increment d'energia, discontinu, continu, KRATOS, CIMNE.

Resum

El Mètode dels Elements Discrets (MED) és una tècnica numèrica que discretitza un material per simular discontinu o continu mitjançant la interacció de grans quantitats d'elements rígids.

L'Aplicació del MED és un codi escrit en C++ del Mètode dels Elements Discrets que està sent desenvolupat dins KRATOS, una plataforma oberta destinada a la implementació de mètodes numèrics per la resolució de problemes d'enginyeria.

Nombrosos models de contacte han estat aplicats en simulacions del MED, però en l'Aplicació de MED hem estat utilitzant el model de molla lineal amb amortidor. La molla lineal genera les forces d'atracció o repulsió entre les partícules, i l'amortidor representa una força d'esmorteïment que actua en el sentit contrari de la velocitat per dissipar energia. Sense ell, qualsevol sistema aniria guanyant energia en cada pas de temps degut als errors de l'esquema d'integració temporal explícit i, per tant, els resultats no tindrien validesa.

El Mètode dels Elements Discrets ha demostrat ser una poderosa i versàtil eina numèrica per la modelització del comportament de sistemes granulars i de partícules, i també per l'estudi de la micromecànica de materials com el sòl a nivell particular. Tot i així, el mètode també té el potencial per esdevenir una eina efectiva per modelitzar problemes continus, especialment aquells caracteritzats per la transformació del continu al discontinu.

En aquest treball es duen a terme diversos experiments amb l'objectiu de validar el codi i verificar les possibilitats actuals de l'Aplicació del MED. Aquests anàlisis inclouen: alguns tests de l'esmorteïment viscós, un model de rellotge de sorra com a exemple de discontinu, i algunes simulacions de continu amb provetes de formigó.

Table of Contents

1. Introduction and Objectives

In the development of any application it is usual to program without thinking of the general public that will be the future users of that work. Furthermore, one can frequently be adding improvements and complex characteristics to the application, but if the basic features do not work properly, that effort is futile.

In this sense, it is crucial that one person works in parallel with the developer, testing and validating the application to report any problem and to know exactly what the application can do and what cannot do.

This thesis contains a collection of the validation works for the DEM Application, performed in CIMNE during my fifth course of Civil Engineering in Barcelona. Its final objective is to help the developers understand the present problems and bugs, and to assess the current potential of the application.

The thesis starts giving a general overview of the Discrete Element Method and the fundamentals behind it in order to introduce the reader to the matter and to make more understandable all the experiments performed.

Following that, I dedicate a brief chapter to present the KRATOS framework, the programming platform in which the DEM Application is developed, and to show the tools that GID offers to prepare the tests.

After these first introductory chapters, it is presented the validation of the viscous damping, one of the most relevant implementations that will be present in all the tests.

The two next chapters show the results of all the work of this last this year through the applications of DEM in discontinuum and continuum problems. In the first place, we are going to see the case of a sand clock modelled with DEM as a discontinuum application of DEM. Then, we go on to continuum experiments with the simulations of three laboratory tests very common in the field of civil engineering: the Uniaxial Compression Strength Test, the Indirect Tensile Strength Test, and the Triaxial Compression Strength Test.

Finally, I state the next steps in the development of the application through the present and future lines of research on the matter.

2. Overview of the Discrete Element Method

The Discrete Element Method (DEM) is a numerical technique that was originally developed by Cundall and Strack (1979) for predicting the behaviour of soil grains. Increasing availability of computing power over the past three decades, along with refinements and adaptations of the original method has made DEM applicable to a wide range of industries. Examples include: pneumatic conveying and particulate flow in pipes, discharging of hoppers, milling, powder mixing and fluidised beds, to name but a few.

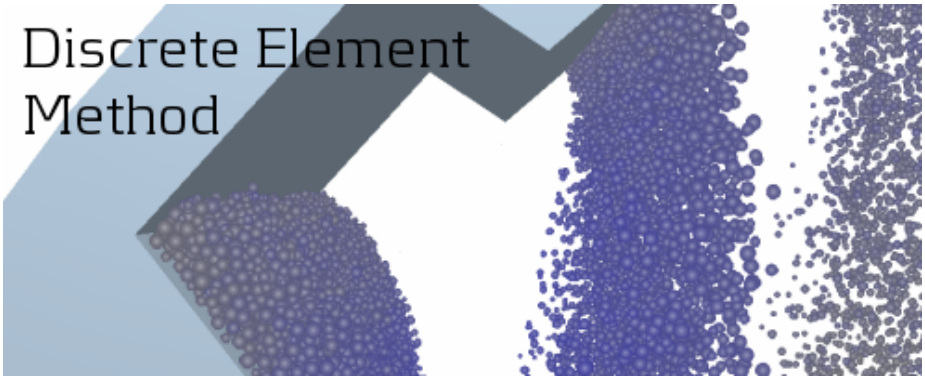

Fig. 1. Discrete Element Method.

Materials are represented as assemblies of particles, each of which may interact with neighbouring particles or other objects (such as planar walls) via simplified force-displacement interaction laws.

For the so-called soft-sphere DEM simulations, the trajectory and rotation of each particle in a system are obtained using a numerical time integration scheme. The contact forces are evaluated at each time step and are resolved into normal and tangential components. Newton's second law of motion is then applied to determine the motion of each particle from any unbalanced forces.

Depending on the application of interest, many thousands or even millions of particles may be required and simulations may consist of up to millions of time steps. The heavy computational burden of the DEM relative to other numerical methods is often the single most limiting factor determining the quality and utility of simulation results.

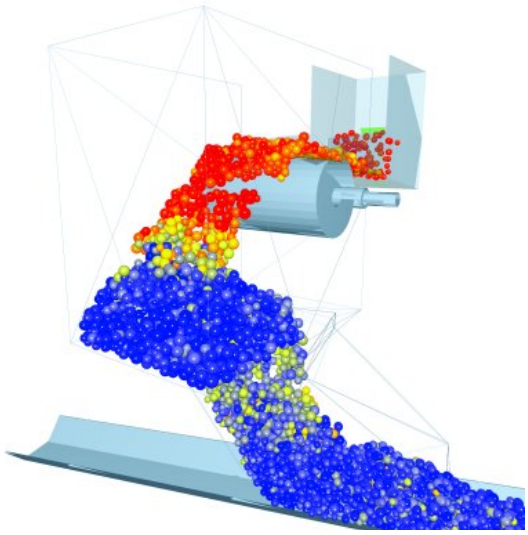

Fig. 2. DEM model of conveyor transport of particles.

Several methods have been used to reduce the computational load of DEM and allow larger number of particles to be simulated within a reasonable timescale. These include the use of more advanced contact detection algorithms; parallel computing techniques, novel numerical time integration schemes, and more commonly in the case of simple linear-spring-dashpot models, selecting a small value of the particle spring constant or stiffness which permits a larger time step to be used. While this latter approach is a simple means of reducing the overall computation time required for a given simulation, it also has the effect of increasing the inter-particle overlap that occurs during collisions.

There are various approaches of the Discrete Element Method, with different element shapes, integration schemes, etc. In this work we are going to focus on the DEM application that is being developed in CIMNE, and the following chapters will all be oriented to it.

3. Fundamentals of DEM

The Discrete Element Method discretizes a material to simulate discontinuum or continuum through the interaction of large amounts of rigid elements. These elements can have different shapes, such as polyhedral, ellipsoidal and spherical, being the latter the most implemented because of its simplicity and speed of the contact detection algorithm.

Since in CIMNE we have been using spheres as discrete elements, from now on I am going to give examples and explanations of the method referring to spherical particles.

Having defined the geometry to analyse, the size of the elements that will conform it, the boundary conditions and the properties of the material, the process involved in the resolution of the method is quite simple.

Three main steps, cyclically repeated, compose this procedure: the contact search, the evaluation of forces and the integration of motion equations.

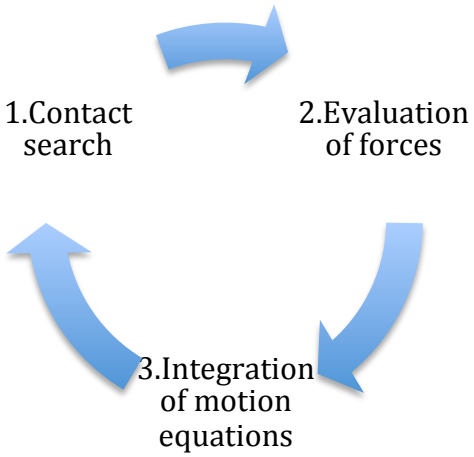

Fig. 3. Main cycle of the process involved in DEM.

Therefore, in a DEM analysis, the interaction of the elements is treated as a dynamic process that alternates between the application of Newton's second law and the evaluation of a force–displacement law at the contacts. Newton's second law gives the acceleration of an element resulting from the forces acting on it, including gravitational forces, external forces prescribed by boundary conditions, and internal forces developed at the contacts. The acceleration is then integrated to obtain the velocity and displacement.

3.1. Contact search

In contrast with the Finite Element Method, in the DEM there are no connections between the nodes by means of the elements. The contact is determined when one body belonging to a discrete element intersects with another body that defines another discrete element.

For every particle and after a prefixed number of time steps, a contact search is carried out in order to set as neighbours those elements that are near enough of the particle in question. The user predefines the distance until which a particle is considered neighbour.

This search allows us to identify the position and determine other characteristics of the neighbours of any element, which are necessary for all the following calculations.

The contact search is a crucial part of the method in terms of computational cost (from 60% to 90% of simulation time), and it is possibly the most difficult part to treat when we deal with particles that have no spherical shape. Thereby, it is logical to perform this search only after a reasonable number of time steps if the time step is small enough.

The contact detection strategy can be divided in two basic stages:

- Global Contact Search: It consists on locating the list of potential contact objects for each given target body. There are two different basic schemes: the Grid/Cell based algorithms and the Tree based ones. There are numerous methods and variations for each type.

    - Grid based algorithm: A general rectangular grid is defined in the entire domain, an unified bounding box or sphere is adopted to represent the discrete elements; the potential contacts are determined by selecting the surrounding cells where each target body is centred on.

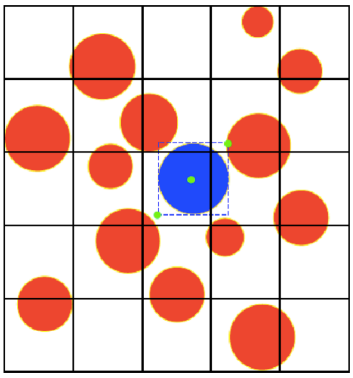

Fig. 4. Scheme of a grid based algorithm.

    - Tree based algorithm: each element is represented by a point. Starting from a centred one, it splits the domain in two sub domains obtaining points that have larger ‘x’ coordinate in one sub domain and points with smaller values of ‘x’ in the other sub domain. We proceed for next points alternating every time the splitting dimension and we obtain a tree structure like the one shown in the figure. Once the tree is constructed for every particle, the nearest neighbours have to be determined following the tree in upwind direction.

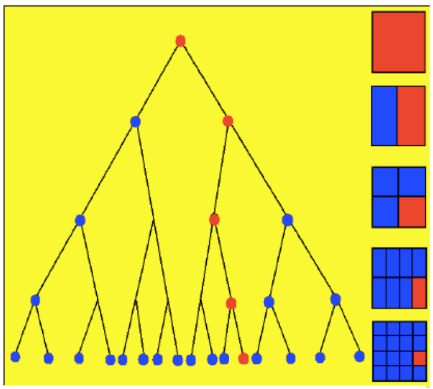

Fig. 5. Scheme of a tree based algorithm.

- Local Resolution Check: The objective is to establish the actual contact configuration. Starting from the potential contacts or areas found in the global contact search, now we enter into detail. This is the difficult and expensive part of the contact detection; even for simple polygonal shapes the detection criteria is not trivial. The complexity is much higher for three-dimensional cases, which are the most frequent ones.

For both, the grid based algorithm and the tree based one, the number of operations needed is of the order $\mathcal{O}(n \cdot \log(n))$, where n is the number of elements.

The brute force search, a method that does a loop for all the elements, computes the minimum distance between each pair, and judges whether there is contact or not, needs a number of operations of the order $\mathcal{O}(n^2)$.

3.2. Evaluation of forces

In order to understand the process involved in the computation of the forces, we must first introduce the contact model used in the Discrete Element Method.

Many different contact models have been applied in DEM simulations. As well as the widely used spring-dashpot models, more complex models have also been proposed. In general, these complex models are more computationally intensive to run, and yet still have to assume smooth contact surfaces and uniform material properties and hence have not been able to see widespread use in DEM simulations. In this work we focus on the linear-spring-dashpot model.

The forces originated by this model are computed in the three local directions of any contact and their definition depend on whether they are normal or tangent.

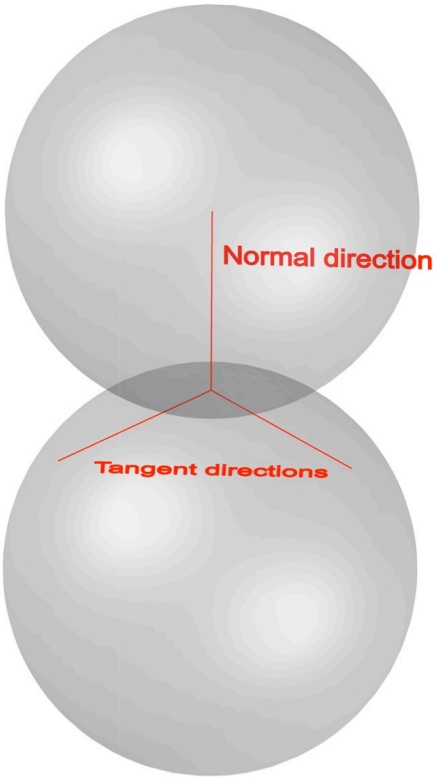

Fig. 6. Scheme of the three local directions of any contact.

Normal direction

The normal contact is modelled by a linear-spring-dashpot system that can be represented in a schematic way as follows.

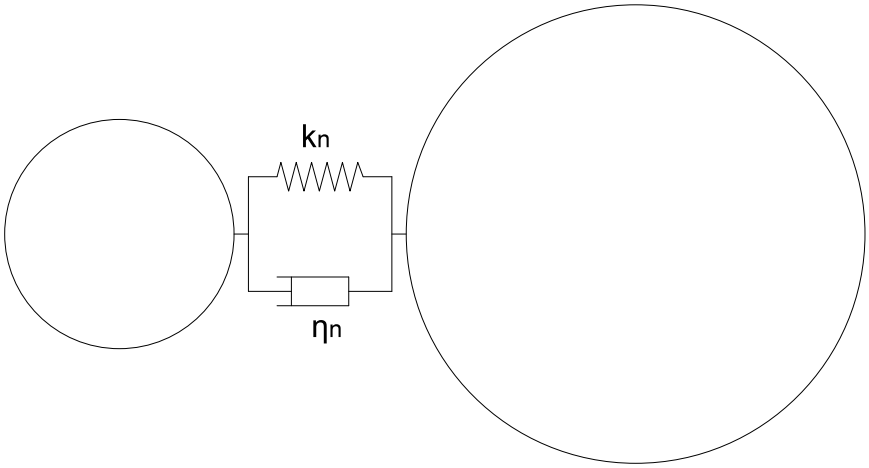

Fig. 7. Scheme of the normal contact between two spherical particles.

Considering the Hook's law, the force of the normal spring between two neighbouring spheres, F_{sn}, is directly proportional to the normal spring constant or normal stiffness, k_n, and the relative displacement of the particles in the normal direction, δ, or the deformation of the theoretical spring, ΔL:

$$F_{sn} = k_n\delta = k_n\Delta L \qquad \text{(Eq. 1)}$$

The application of this force and the value of the stiffness depend on whether we are simulating continuum or discontinuum. However, we can start introducing the basis of their common characteristics.

In order to understand the meaning of the deformation of the spring, we can consider an ideal case in which two neighbouring spheres are tangentially in contact and connected with a spring.

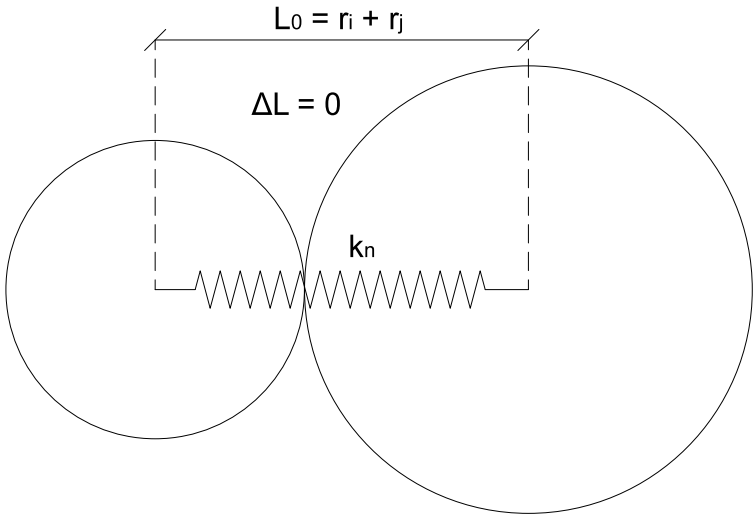

Fig. 8. State of equilibrium of the normal spring between two neighbours.

The deformation of the spring will be the relative displacement between the two spheres and it can be easily calculated from the coordinates of the centre of each sphere and their radiuses. Its value can be either positive or negative.

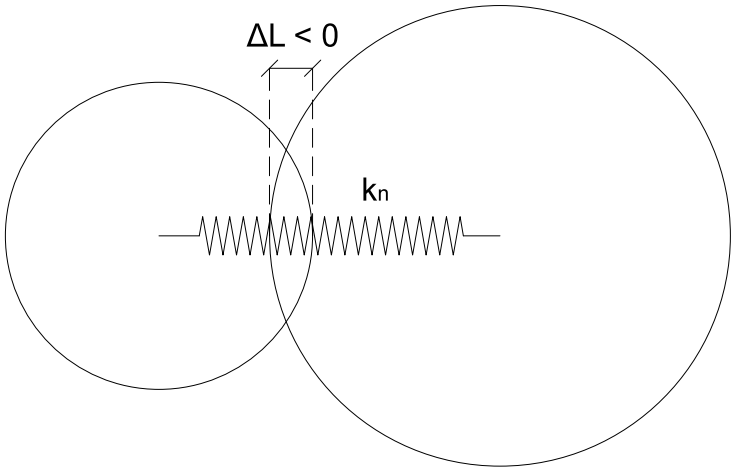

Fig. 9. Scheme of the spring when the particles get closer.

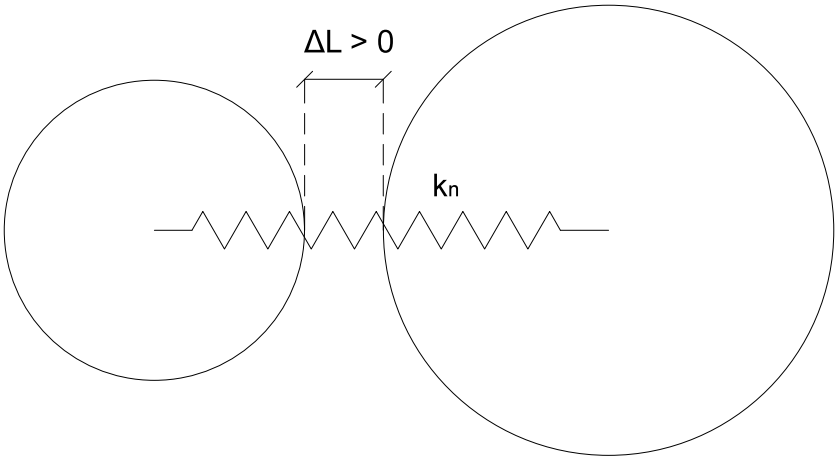

Fig. 10. Scheme of the spring when the particles get farther.

One must notice that the pictures above represent an ideal case that would only be possible with simulations of an infinite number of spheres. Therefore, due to meshing limitations, we will not normally find neighbouring spheres tangentially in contact. Instead, we will have some neighbouring particles initially separated by a gap and some others already indented.

This circumstance is actually taken into account in the code, and it is basically solved by considering the initial distance between two neighbours as the equilibrium length of the spring.

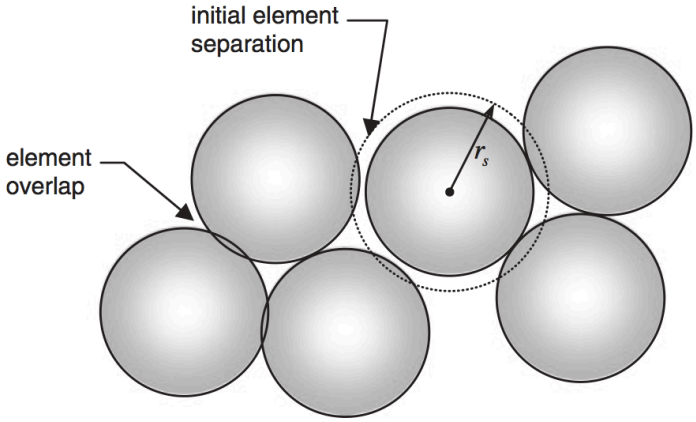

Fig. 11. Scheme of a set of particles in a more realistic case.

By the way, the computation of the stiffness coefficient between each pair of neighbouring spheres implies a series of suppositions that must be explained.

We first must obtain the stiffness coefficient formula, considering the following relations:

- The Hook's law: $F_{sn} = k_n \Delta L$
- The constitutive law: $\sigma = E\varepsilon$

- The definition of the stress: $\sigma = \frac{F_{sn}}{A}$
- The definition of the strain: $\varepsilon = \frac{\Delta L}{L_0}$

Now we can regroup terms and isolate the stiffness parameter:

$F_{sn} = A\sigma \rightarrow k_n \Delta L = AE\varepsilon \rightarrow k_n \Delta L = AE\frac{\Delta L}{L_0}$ and so:

$$k_n = \frac{EA}{L_0} \qquad \text{(Eq. 2)}$$

The Young modulus, E, is a known variable that depends on the material we are working with; and the length of the spring is the sum of the radius of the two spheres: $L_0 = r_i + r_j$.

For discontinuum simulations, we have considered the contact area A between two neighbouring spheres as an equivalent area of a circle of radius r_e like the one showed in the figure.

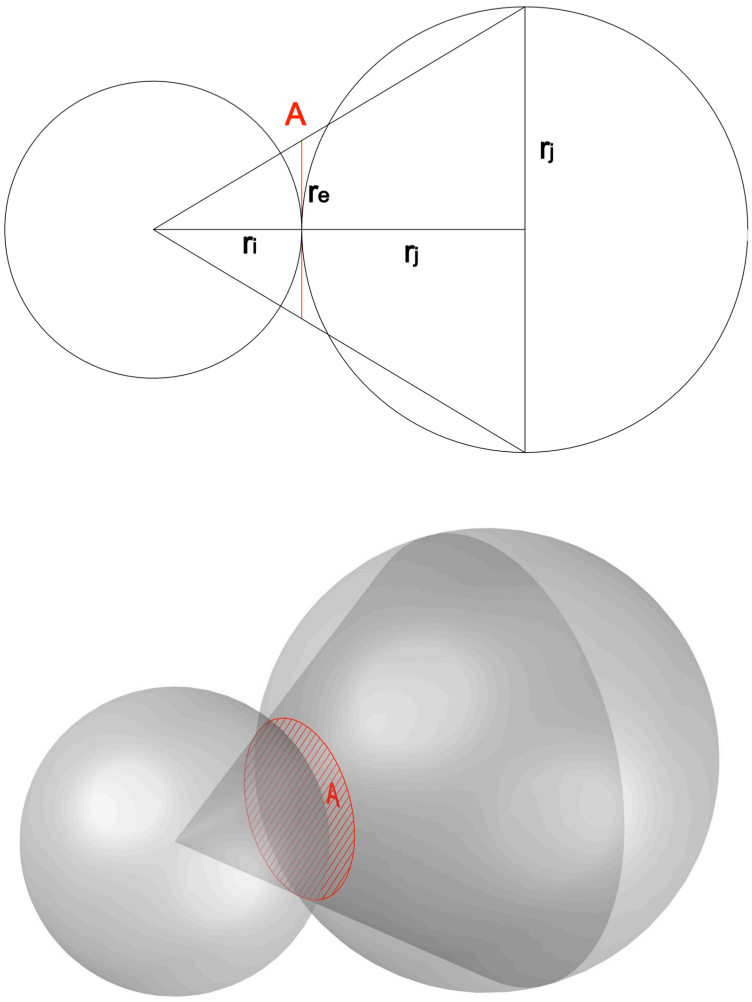

Fig. 12. Considered contact area in discontinuum cases.

By proportionality we obtain the value of the radius r_e:

$$r_e = \frac{r_i r_j}{r_i + r_j} \qquad \text{(Eq. 3)}$$

Thereby, the contact area depicted in red is:

$$A = \pi r_e^2 = \pi \left(\frac{r_i r_j}{r_i + r_j} \right)^2 \qquad \text{(Eq. 4)}$$

For continuum, this value of area will be affected by a corrector coefficient that will be explained in the corresponding chapter.

Finally, the linear-spring constant for discontinuum results:

$$k_n = \frac{EA}{L_0} = E\pi \left(\frac{r_i r_j}{r_i + r_j} \right)^2 \frac{1}{r_i + r_j} = \frac{E\pi (r_i r_j)^2}{(r_i + r_j)^3} \qquad \text{(Eq. 5)}$$

If the contact was modelled using only this linear-spring, no energy would be consumed and the contact would be perfectly elastic. In reality, however, some kinetic energy is dissipated in plastic deformation, and/or converted to heat or sound energy. In order to take into account this, a contact damping force based on a dashpot model is also included:

$$F_{dn} = \eta_n v \qquad \text{(Eq. 6)}$$

The normal damping force, F_{dn}, is proportional to the relative velocity of the particles in the normal direction, v, and the normal damping coefficient, η_n, and always acts with the opposite sign of the velocity.

The velocity of each particle is computed at every time step by solving the Newton's second law with an explicit time integration scheme, as we will see afterwards.

Regarding the damping coefficient, it is a common practice to base its value on the collisional properties of the simulated materials, in particular, on the coefficient of restitution e. From Newton's law of restitution (Wang & Mason, 1992), e is defined as:

$$e = \left| \frac{v_1}{v_0} \right| \qquad \text{(Eq. 7)}$$

Where v_0 and v_1 are the normal components of relative velocity at the contact point before and after a collision.

Strictly speaking, the coefficient of restitution is not a material property, not yet a constant for any given material; it depends on the relative impact velocity of the colliding particles (Kuwabara & Kono, 1987). However, variation of e with impact

velocity has been shown to be significant only at high impact velocities (of order 10 m/s and above) (Labous, Rosato, & Dave, 1997), and for practical purposes the coefficient of restitution is often taken to be a constant in DEM simulations, irrespective of impact velocity.

For the linear-spring-dashpot model, a relationship between the damping coefficient, η_n, and the coefficient of restitution, e, may be derived from the solution of the equation resulting from the application of Newton's second law of motion to a particle i at any time t:

$$m_i \frac{dv_i}{dt} = \sum_{j=1}^{k_i} \left(F_{sn,ij} + F_{dn,ij}\right) + m_i g + F_i \qquad \text{(Eq. 8)}$$

Where m_i is the mass of particle i, v_i is its translational velocity, and k_i is the number of particles in contact with i at time t.

The right-hand side of the equation represents the forces acting on the particle. These include the contact force, $F_{sn,ij}$, and the contact damping force, $F_{dn,ij}$, between particles i and j; the gravitational force, $m_i g$; any other forces, F_i, that may act on particle i due to, for instance, interparticle cohesion, electromagnetic effects, or fluid-particle interactions.

If we substitute the expressions of F_{sn} and F_{dn} into the equation and neglect $m_i g$ and F_i terms, we obtain the following equation of motion for the particle in the normal direction:

$$m \frac{d^2\delta}{dt^2} + \eta_n \frac{d\delta}{dt} + k_n \delta = 0 \qquad \text{(Eq. 9)}$$

Which is the classical equation of motion for a mass-spring-dashpot system.

Given the initial conditions: $t = 0 : \delta = 0; \dot{\delta} = v_0$, the solution of the equation for the so-called underdamping conditions (Kreyszig, 2006), $\eta_n^2 < 4mk_n$, is:

$$\delta = \frac{v_0}{\omega} \exp\left(-\frac{\eta_n}{2m} t\right) \sin(\omega t) \qquad \text{(Eq. 10)}$$

and

$$\dot{\delta} = \frac{v_0}{\omega} \exp\left(-\frac{\eta_n}{2m} t\right) \left[\omega \cos(\omega t) - \frac{\eta_n}{2m} \sin(\omega t)\right] \qquad \text{(Eq. 11)}$$

where $\omega = \sqrt{4mk_n - \eta_n^2/2m}$.

From (Eq. 11), we obtain the following relation for e:

$$e = \exp\left(\frac{-\pi\eta_n}{\sqrt{4mk_n - \eta_n^2}}\right) \qquad \text{(Eq. 12)}$$

Rearranging this latter equation to obtain η_n as a function of e gives the result

presented by Ting, Corkum, Kauffman, and Greco (1989):

$$\eta_n = \frac{2(\ln e)\sqrt{mk_n}}{\sqrt{(\ln e)^2+\pi^2}} \qquad \text{(Eq. 13)}$$

The limit of this function, as $e \rightarrow 0$, is $\eta_n = -2\sqrt{mk_n}$. If η_n takes this value, the system is critically damped, and there will be no rebound.

Tangential directions

The tangential contact is also modelled by the same linear-spring-dashpot system but with different parameters:

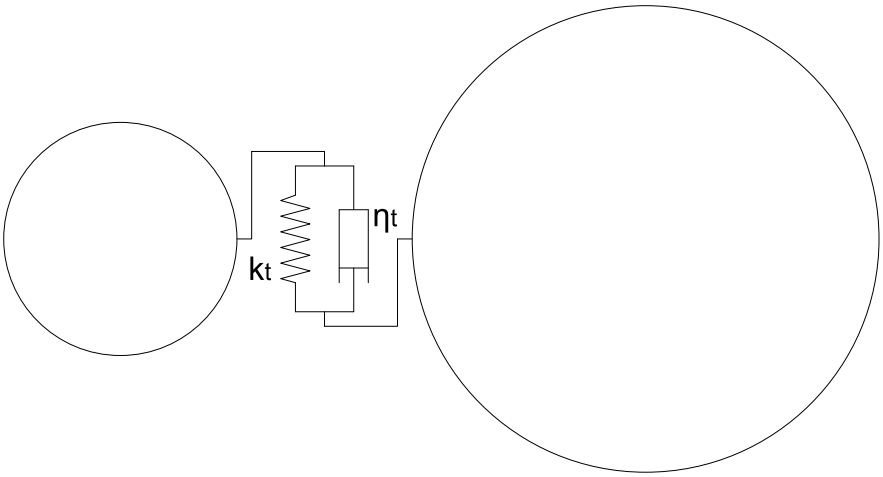

Fig. 13. Scheme of the tangential contact between two spherical particles.

The stiffness coefficient for the tangential spring, k_t, is computed considering that:

$$\frac{k_n}{k_t} = \frac{E}{G} \qquad \text{(Eq. 14)}$$

Where G denotes the shear modulus, $G = \frac{E}{2(1+\nu)}$, and ν the Poisson's ratio.

Therefore, k_t is:

$$k_t = \frac{k_n}{2(1+\nu)} \qquad \text{(Eq. 15)}$$

Moreover, the damping coefficient for the tangential dashpot, η_t, is calculated with the same formula as in the normal direction, but changing k_n by k_t:

$$\eta_t = \frac{2(\ln e)\sqrt{mk_t}}{\sqrt{(\ln e)^2+\pi^2}} \qquad \text{(Eq. 16)}$$

3.3. Integration of motion equations

After having calculated all the forces acting on a particle at a specific time step, the displacement and the velocity are obtained by solving the translational Newton's second law:

$$\sum \mathbf{F} = \mathrm{m}\mathbf{a} \qquad \text{(Eq. 17)}$$

Where **F** is the forces vector, m the particle mass, and **a** the acceleration vector.

Furthermore, if the particles are given a rotational inertia, we can compute its rotation by integrating the Euler's equations for rigid body:

$$\mathrm{I}_1\dot{\omega}_1 + (\mathrm{I}_3 - \mathrm{I}_2)\omega_2\omega_3 = \mathrm{M}_1 \qquad \text{(Eq. 18)}$$

$$\mathrm{I}_2\dot{\omega}_2 + (\mathrm{I}_1 - \mathrm{I}_3)\omega_3\omega_1 = \mathrm{M}_2 \qquad \text{(Eq. 19)}$$

$$\mathrm{I}_3\dot{\omega}_3 + (\mathrm{I}_2 - \mathrm{I}_1)\omega_1\omega_2 = \mathrm{M}_3 \qquad \text{(Eq. 20)}$$

Where I_i are the principal moments of inertia, ω_i are the components of the angular velocity along the principal axes, and M_i are the components of the applied torques.

For a spherical particle with $I_1=I_2=I_3=I$ we can rewrite the Euler's equations as:

$$\sum \mathbf{M} = \mathrm{I}\boldsymbol{\alpha} \qquad \text{(Eq. 21)}$$

Where **M** is the torques vector, I the moment of inertia, and **α** the angular acceleration vector.

We need an adequate time integration scheme to solve efficiently both equations.

A wide range of time integration schemes is available in the literature. However, it is generally agreed that explicit methods are better for DEM simulations because of its simplicity in terms of computational cost, structure and memory requirements. On the other hand, this kind of method is conditionally stable, which implies the use of a suitable time step to work properly.

Rougier, Munjiza, and John (2004) have compared 12 explicit time integration schemes for an ideal one-degree-of-freedom mass-spring system. The results favour the use of lower-order schemes in terms of accuracy, stability and CPU efficiency provided an appropriate time step.

A number of authors have suggested guidelines to calculate the maximum time step that may be used for popular lower-order schemes, based on the properties of the particles in the system. It is commonly accepted that the time step should be less than a certain critical value, which is usually expressed as a fraction of the natural frequency of the equivalent mass-spring system. However, the exact fraction of the natural frequency and indeed the relation used to obtain the natural

frequency can differ significantly between authors.

It has become common practice in DEM modelling of particulate systems to use a relation of the form:

$$\Delta t \leq C\sqrt{m/k} \qquad \text{(Eq. 22)}$$

for selecting the time step, where C is a constant, m the particle mass, and k the stiffness.

Forward Euler Scheme

Forward Euler is the most used explicit time integration scheme in DEM-application of KRATOS in CIMNE. The basis of the method can be easily shown through the integration of the translational Newton's second law:

$$\sum \mathbf{F} = m\mathbf{a} \leftrightarrow \sum \mathbf{F} = m\frac{d\mathbf{v}}{dt} \leftrightarrow \frac{d\mathbf{v}}{dt} = \frac{\sum \mathbf{F}}{m} \qquad \text{(Eq. 23)}$$

At a time step t_i, the equation to be solved is:

$$\frac{d\mathbf{v_i}}{dt} = \frac{\sum \mathbf{F_i}}{m} \qquad \text{(Eq. 24)}$$

Where $\mathbf{v_i} = \mathbf{v}(t_i)$ and $\mathbf{F_i} = \mathbf{F}(t_i)$.

The idea of the Euler method is to approximate the derivative at the instant t_i with an incremental quotient.

From Taylor's Series, we have:

$$\mathbf{v_{i+1}} = \mathbf{v_i} + \Delta t\frac{d\mathbf{v_i}}{dt} + \mathcal{O}(\Delta t^2) \qquad \text{(Eq. 25)}$$

Where Δt is the time step that the user chooses, and $\mathcal{O}(\Delta t^2)$ is the truncation error.

By regrouping terms, we obtain:

$$\frac{d\mathbf{v_i}}{dt} = \frac{\mathbf{v_{i+1}} - \mathbf{v_i}}{\Delta t} - \mathcal{O}(\Delta t) \qquad \text{(Eq. 26)}$$

If we substitute this result in the equation that has to be solved, we have an equation that verifies the analytical solution:

$$\frac{d\mathbf{v_i}}{dt} = \frac{\mathbf{v_{i+1}} - \mathbf{v_i}}{\Delta t} - \mathcal{O}(\Delta t) = \frac{\sum \mathbf{F_i}}{m} \rightarrow \mathbf{v_{i+1}} = \mathbf{v_i} + \Delta t\frac{\sum \mathbf{F_i}}{m} + \Delta t\,\mathcal{O}(\Delta t) \quad \text{(Eq. 27)}$$

Now, not taking into account the truncation errors $\mathcal{O}(\Delta t)$, we get the numerical scheme of the Euler's method.

$$\mathbf{v_{i+1}} = \mathbf{v_i} + \Delta t \frac{\sum \mathbf{F_i}}{m} \qquad \text{(Eq. 28)}$$

Thereby, from the velocity and the forces at the time step t_i we can obtain the velocity at t_{i+1}.

One must notice that this does not provide an exact solution but an approximation, which accuracy depends on the value of the time step Δt chosen.

Finally, we can obtain the displacement at t_{i+1} by applying the same procedure to the following relation:

$$\frac{d\boldsymbol{\delta_i}}{dt} = \mathbf{v_i} \qquad \text{(Eq. 29)}$$

Once again, from the displacement at the time step t_i we can obtain the displacement at t_{i+1}.

$$\boldsymbol{\delta_{i+1}} = \boldsymbol{\delta_i} + \Delta t\, \mathbf{v_i} \qquad \text{(Eq. 30)}$$

To find out the rotation of the particle we just have to integrate the Euler's equations following the same method than before.

Although in this work we have only been using the Forward Euler scheme, there are other explicit methods that can be used to integrate the motion equations, e.g. Midpoint rule, Newmark-beta method, etc.

4. KRATOS and DEM Application

KRATOS is an Open-Source framework for the implementation of numerical methods for the solution of engineering problems. It is written in C++ and is designed to allow collaborative development by large teams of researchers focusing on modularity as well as on performance. KRATOS features a "core" and "applications" approach where "standard tools" (databases, linear algebra, search structures, etc.) come as a part of the core and are available as building blocks in the development of "applications" which focus on the solution of the problems of interest. Its ultimate goal is to simplify the development of new numerical methods.

Fig. 14. KRATOS' logo.

The DEM Application is one of these KRATOS applications, designed for execution on multi-core Personal Computers, clusters or supercomputers running Linux-based operating systems. The users manage the application through the Problem Type implemented in GID, software for pre and post processing.

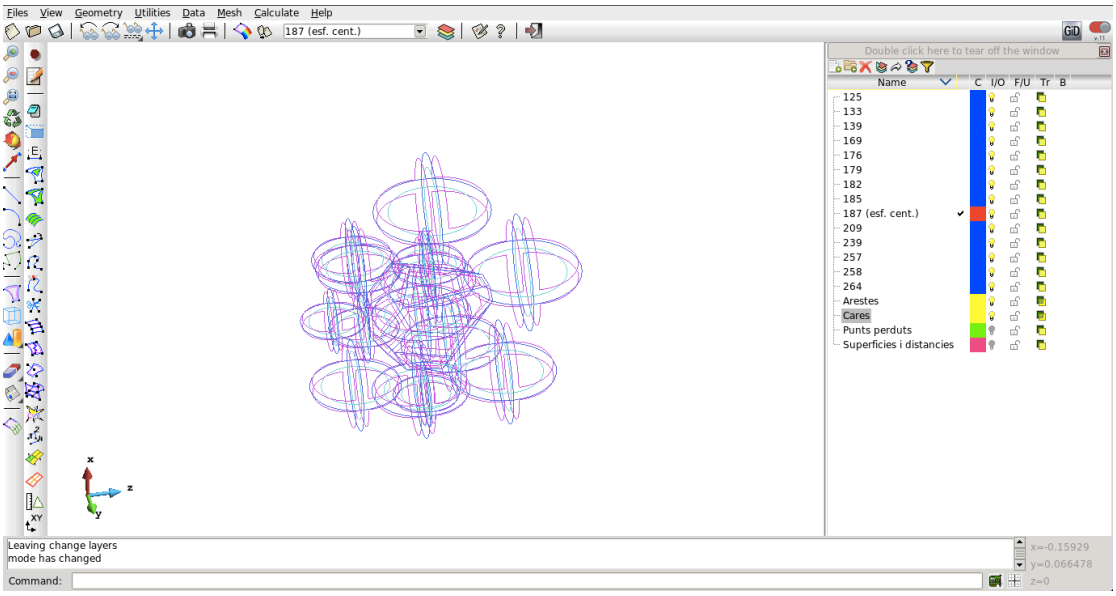

Fig. 15. Interface of Pre-processing of GID.

In this work we will be introducing practical examples of DEM simulations in order to make the explanations more understandable and to perform different tests.

However, first of all we should state the main characteristics of the DEM Application so that we can understand the difficulties found in the performance of these experiments and the reasons behind their designs.

In order to define the geometry of any problem we can:

- Create individual spherical entities with a predefined radius

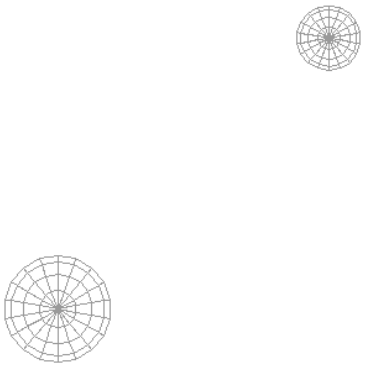

Fig. 16. Mesh of individual spherical entities.

- Fill a line with identical spheres predefining radius and distance

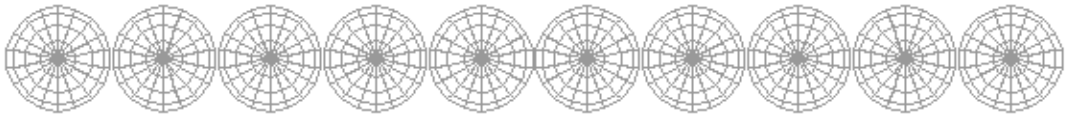

Fig. 17. Uniform mesh of a line with spherical particles.

- Divide a plane with predefined finite elements and fill it with identical spheres of prefixed radius settled at the nodes of these finite elements

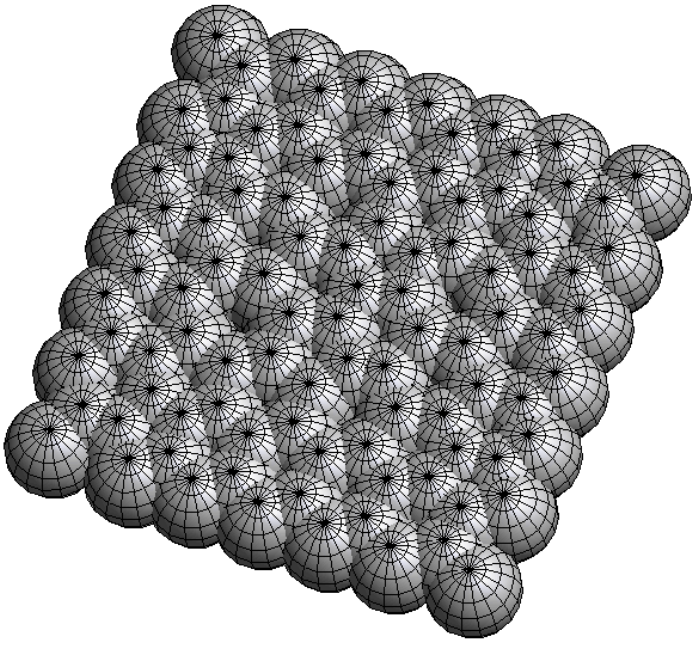

Fig. 18. Uniform mesh of a plane with spheres.

- Divide a volume with predefined finite elements and fill it with identical spheres of predefined radius settled at the nodes of these finite elements

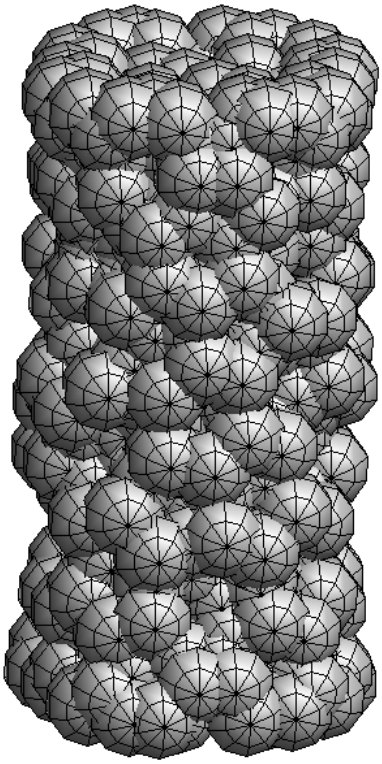

Fig. 19. Uniform mesh of a cylinder with spheres.

- Mesh a predefined volume with a non-uniform distribution of spherical particles of different radius

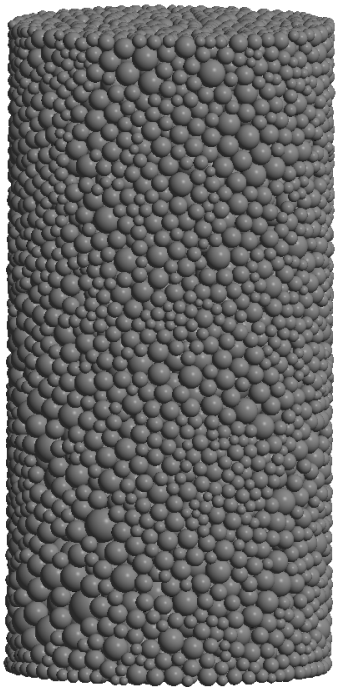

Fig. 20. Non-uniform mesh of a cylinder with spheres.

The boundary conditions of the problem may be predefined by:

- Setting an initial velocity in any direction of the space to any particle
- Setting a fixed velocity in any direction of the space to any particle

To set the material properties of any spherical particle we must:

- Input the particle density
- Input the Young's modulus
- Input the Poisson's ratio
- Input the Dynamic friction angle
- Input the restitution coefficient

The rest of the options to consider are:

- The election of the integration scheme
- The activation of the damping force
- The gravity acceleration in any direction
- The number of steps between each contact search (Search step)
- The total calculation time
- The time step
- The possibility of fixing velocities at predetermined time
- The activation of continuum simulation
- The failure criterion for continuum and the parameters that govern it
- The possibility of applying a confinement pressure
- The activation of the rotation of the spheres

Finally, we should mention an important limitation that must be considered. The application does not allow us to create smooth surfaces that could be very useful for simulating containers, compression plates, etc. Instead, one can only generate them by the accumulation of a great amount of little spheres, which, apart from being inconvenient, increases the total number of particles, and so makes the computation more costly.

5. Viscous damping implementation and test

The dashpot introduced in the contact model plays an essential role in the results obtained from DEM simulations. It represents a contact damping force that acts with the opposite sign of the velocity to dissipate energy. Without it, any system would be gaining energy at every time step because of the errors of the explicit time integration scheme and thus the results would have no validity.

Similarly to what happens when defining the force of the linear spring, the application of the damping force depends on whether we are working with a discontinuum or continuum. In the first case, the damping force is applied when there is overlap between two neighbouring particles. In continuum simulations, however, the damping force appears as long as the contact between two neighbouring particle has not failed. Once it fails, the force is applied when there is overlap between two neighbours, like in discontinuum.

As a reminder, the normal damping force is computed as:

$$F_{dn} = \eta_n v$$

Where v is the relative velocity of the particles, and η_n is the damping coefficient, calculated with the following formula:

$$\eta_n = \frac{2(\ln e)\sqrt{mk_n}}{\sqrt{(\ln e)^2 + \pi^2}}$$

Being m the particle mass, k_n the linear-spring constant and e the restitution coefficient.

As we have already said before, the restitution coefficient is considered as a constant that must be introduced by the user and is defined as:

$$e = \left|\frac{v_1}{v_0}\right|$$

Where v_0 and v_1 are the normal components of relative velocity at the contact point before and after a collision.

One must understand the restitution coefficient as an approximate means to indicate the percentage of loss of energy in the system due to the damping force. Therefore, it only makes sense for $|v_1| \leq |v_0|$ or, equivalently, when $0 \leq e \leq 1$, which implies that the damping coefficient η_n is always negative and, consequently, the damping force has always the opposite sign of the velocity.

Thereby, a restitution coefficient of value 0 implies that the system is critically damped, there will be no rebound, and the damping coefficient is computed as $\eta_n = -2\sqrt{mk_n}$. When e = 1, η_n becomes 0 and so the damping force does not act; and intermediate values of the restitution coefficient lead to the application of

damping forces that dissipate a certain percentage of the energy.

In order to understand the importance of the viscous damping, we have carried out some simple tests that show clearly the effect of its implementation.

5.1. Evolution of mechanical energy when no damping is applied

The aim of this experiment is to evidence the increment of mechanical energy that miscalculations of the method induce when no damping force is introduced. Furthermore, we will see the effect of the stiffness of the contact and the time step on the accuracy of the solution.

The miscalculations in DEM simulations due to the explicit time integration scheme can be easily understood from the analysis of the mechanical energy in the simple case of a spherical particle that freely fall from a determined height under the gravity force, and bounce over a fixed sphere.

The mechanic energy is calculated as the addition of the gravitational potential energy, the kinetic energy and the elastic potential energy of the particle.

$$E_m = E_g + E_k + E_e \qquad \text{(Eq. 31)}$$

The gravitational potential energy is computed as $E_g = mgh$, where m is the particle mass, g is the gravity (9,81 m/s^2), and h is the height of the moving sphere respect the fixed one.

The kinetic energy is obtained from $E_k = \frac{1}{2}mv^2$, where v is the velocity of the free sphere.

The elastic potential energy is the energy of the linear spring of each contact, and it is calculated as $E_e = \frac{1}{2}k_n\delta^2$, where δ is the deformation of the spring of the contact or the overlap between each pair of spheres due to the collision, and k_n is the stiffness coefficient of the spring.

$$k_n = \frac{E\pi(r_i r_j)^2}{(r_i + r_j)^3}$$

Where E is the Young's Modulus and r_i, r_j are the radius of each pair of spheres.

Theoretically, if the air friction is neglected, like in this example, the mechanical energy of the system should be the same all the time.

Analysing the mechanical energy through time we have that, initially, the spherical particle must have only gravitational potential energy due to the height, $E_{m0} = E_{g0}$. At the instant just before the collision, all the gravitational energy must have been transformed into kinetic energy, $E_{m1} = E_{k1}$. Finally, all the kinetic energy must be

transformed into elastic potential energy when the spherical particle is motionless and indented in the fixed sphere, $E_{m2} = E_{e2}$.

Consequently, for an initial height $h_0 = h$, there should be a maximum velocity $v_1 = v_{max}$, and a maximum deformation of the spring $\delta_2 = \delta_{max}$ that accomplish the conservation of the mechanical energy or, equivalently, that make $E_{g0} = E_{k1} = E_{e2}$. Nevertheless, if the predefined time step is not small enough, the particle can gain a certain amount of energy after every rebound.

This happens because the maximum deformation of the spring previously mentioned is exceeded, $\delta_2 > \delta_{max}$, the normal contact force then is larger than the necessary to bring the particle back to the initial height, and thus the mechanical energy increases.

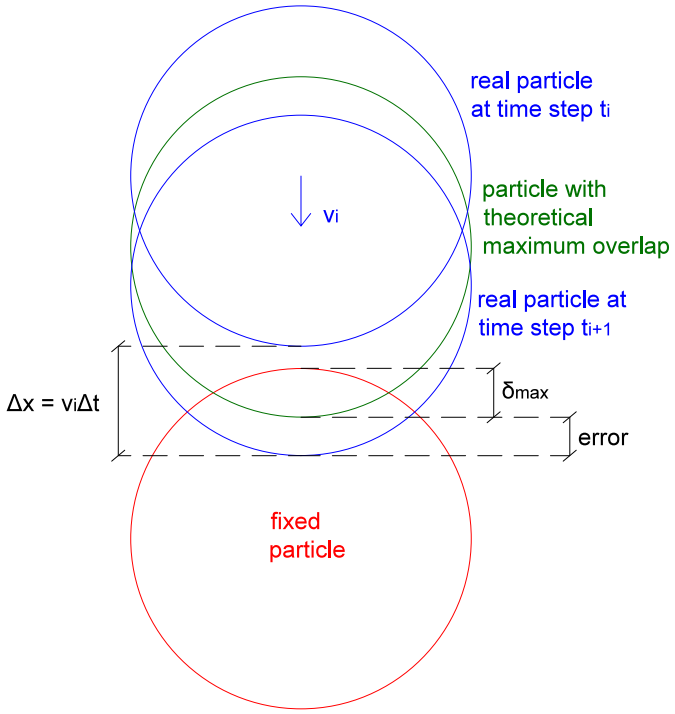

Fig. 21. Scheme of the appearance of the error.

The objective of the experiment is to obtain the percentage of energy that a sphere gains after any collision, and see how it changes in terms of the stiffness and the time step. In order to minimize errors and to obtain a more representative result, we have performed the test for ten identical spherical particles that fall from different heights and we have computed the average percentage of energy increment after every rebound.

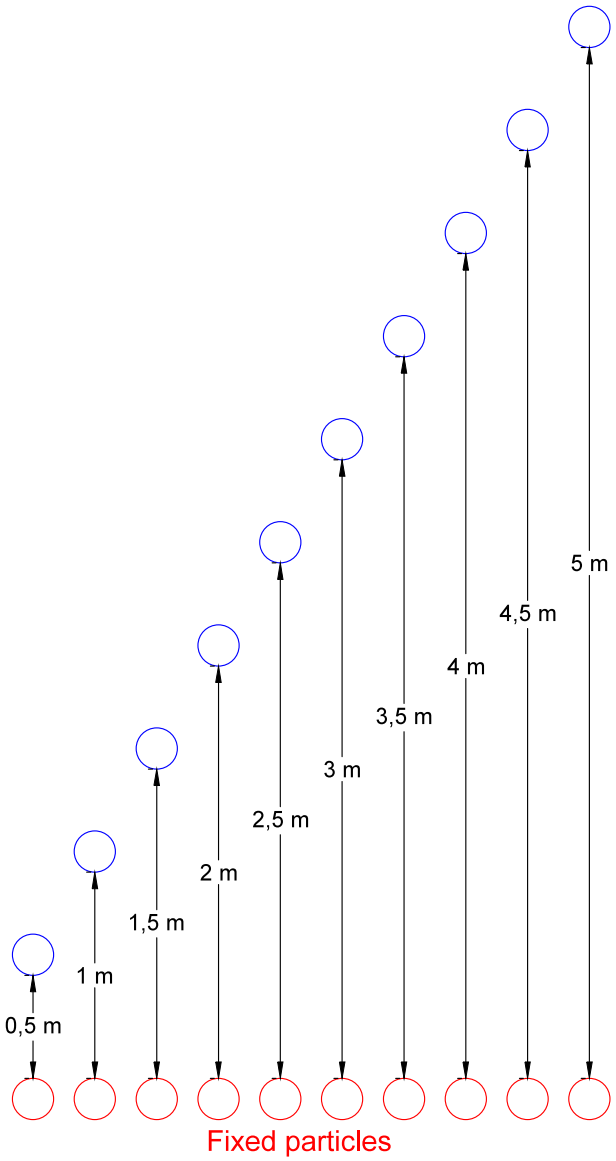

Fig. 22. Scheme of the initial position of all the spheres.

Moreover, we have computed the maximum overlap after any collision between to spheres as a percentage of their radius. Once again, we have obtained an average from all the collisions.

The common characteristics of the experiment are the following:

Geometry and Material	
Particle Radius	0,1 [m]
Particle Density	100 [Kg/m^3]
Restitution Coefficient	1,0
Problem Data	
DEM simulation	Discontinuum
Integration Scheme	Forward Euler
Search Step	10
Simulation Time	6 [s]

Table 1. Characteristics of the damping test 1.

The results of the test have been summarized in the following table:

Δt = 0,0001 s		
E [N/m^2]	Overlap (% of radius)	ΔE_m (%)
$1{,}0 \cdot 10^5$	65,787	0,211
$1{,}0 \cdot 10^6$	21,110	2,009
$1{,}0 \cdot 10^7$	8,884	29,195
$1{,}0 \cdot 10^8$	5,193	244,791
$1{,}0 \cdot 10^9$	3,648	2130,089
Δt = 0,00005 s		
E [N/m^2]	Overlap (% of radius)	ΔE_m (%)
$1{,}0 \cdot 10^5$	65,669	0,070
$1{,}0 \cdot 10^6$	20,716	0,637
$1{,}0 \cdot 10^7$	6,979	6,276
$1{,}0 \cdot 10^8$	3,475	77,395
$1{,}0 \cdot 10^9$	3,174	1051,524
Δt = 0,00001 s		
E [N/m^2]	Overlap (% of radius)	ΔE_m (%)
$1{,}0 \cdot 10^5$	65,610	0,004
$1{,}0 \cdot 10^6$	20,541	0,028
$1{,}0 \cdot 10^7$	6,495	0,264
$1{,}0 \cdot 10^8$	2,143	3,280
$1{,}0 \cdot 10^9$	0,893	30,835

Table 2. Results of the damping test 1.

Graphically, we have:

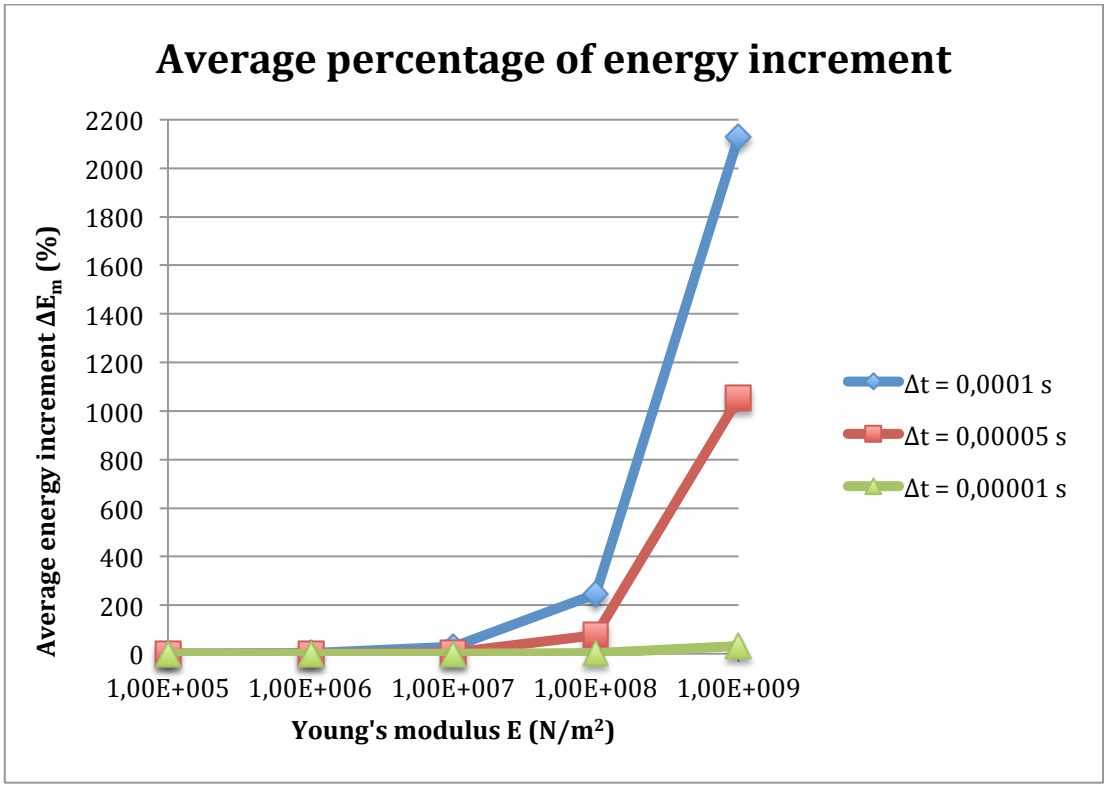

Fig. 23. Average percentage of energy increment.

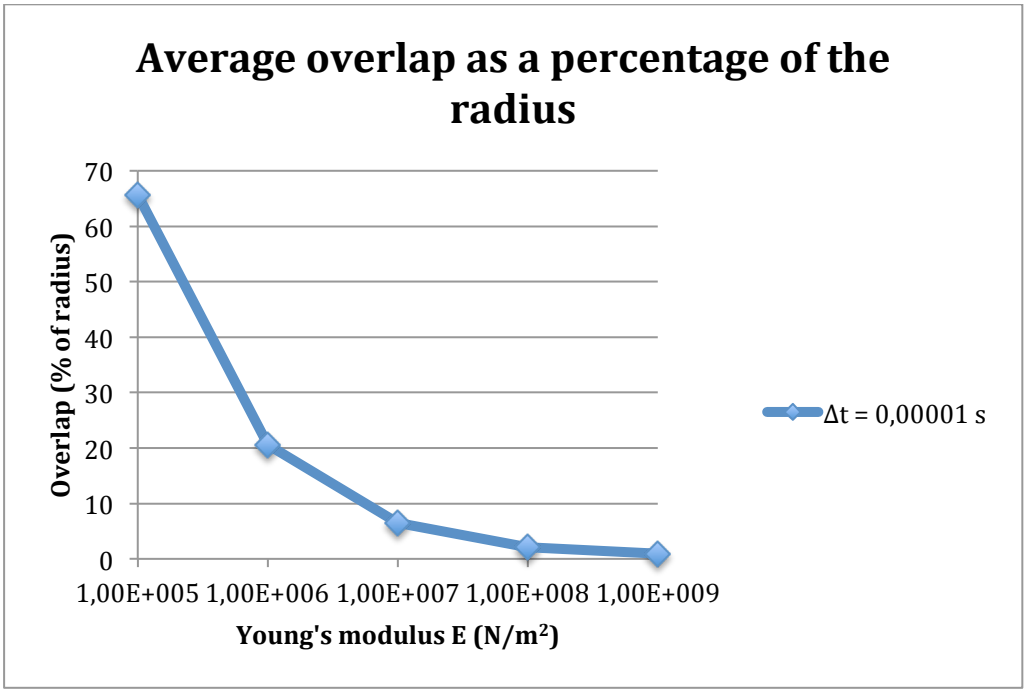

Fig. 24. Average overlap as a percentage of the radius.

Therefore, with a fixed time step, as the stiffness of the spring increases, the maximum overlap after every collision decreases, the indentation errors are larger and thus the energy increment becomes greater.

On the other hand, with a fixed Young's modulus, as the time step increases, the system gains more energy after every rebound because the solution is less accurate.

5.2. Effect of the normal damping

In this case, we have performed the previous test again, but we have been varying the restitution coefficient from 1 to 0, in order to see the repercussion of the normal damping force on the mechanical energy.

The main properties used to perform this test are:

Geometry and Material	
Particle Radius	0,1 [m]
Particle Density	100 [Kg/m^3]
Young's Modulus	$1{,}0 \cdot 10^7$ [N/m^2]
Problem Data	
DEM simulation	Discontinuum
Integration Scheme	Forward Euler
Search Step	10
Simulation Time	6 [s]
Time Step	0,00005 [s]

Table 3. Characteristics of the damping test 2.

The results are shown in the next table:

Restitution Coefficient	ΔEm (%)
1	6,28
0,9	-10,05
0,8	-30,57
0,7	-46,83
0,6	-61,43
0,5	-72,22
0,4	-81,54
0,3	-89,80
0,2	-95,13
0,1	-98,74
0,0	-100,00

Table 4. Results of the damping test 2.

In a graph:

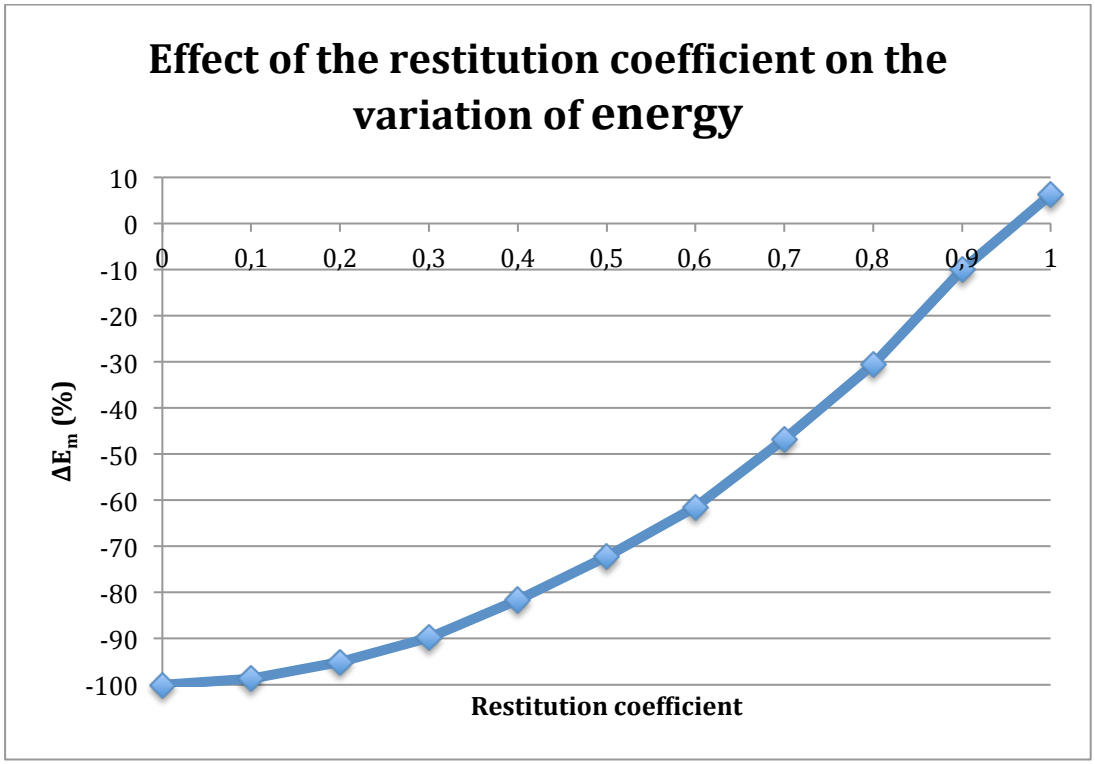

Fig. 25. Effect of the restitution coefficient on the variation of energy.

Thereby, as it is mentioned before, the restitution coefficient is an approximate means to indicate the percentage of energy loss by the system. We can see that the extreme value 0 implies a complete loss of energy or no rebound in the example.

Moreover, we can take a look now at one of the ten particles bouncing and see the evolution of its mechanical energy in terms of time for different values of the restitution coefficient. For instance, if we choose the particle that falls from an initial height of 1,5 m, the resulting energy graphs are as follow:

For a restitution coefficient of 1:

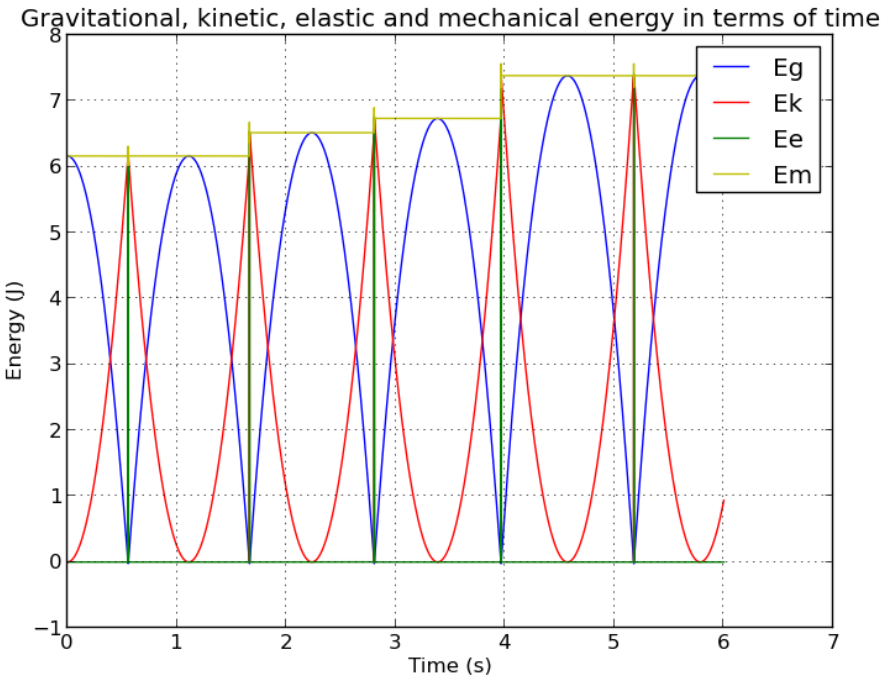

Fig. 26. Energy - time with a restitution coefficient of 1.

As we had seen before, with no damping force the sphere gains energy after every rebound due to the miscalculations of the explicit method.

For a restitution coefficient of 0,5:

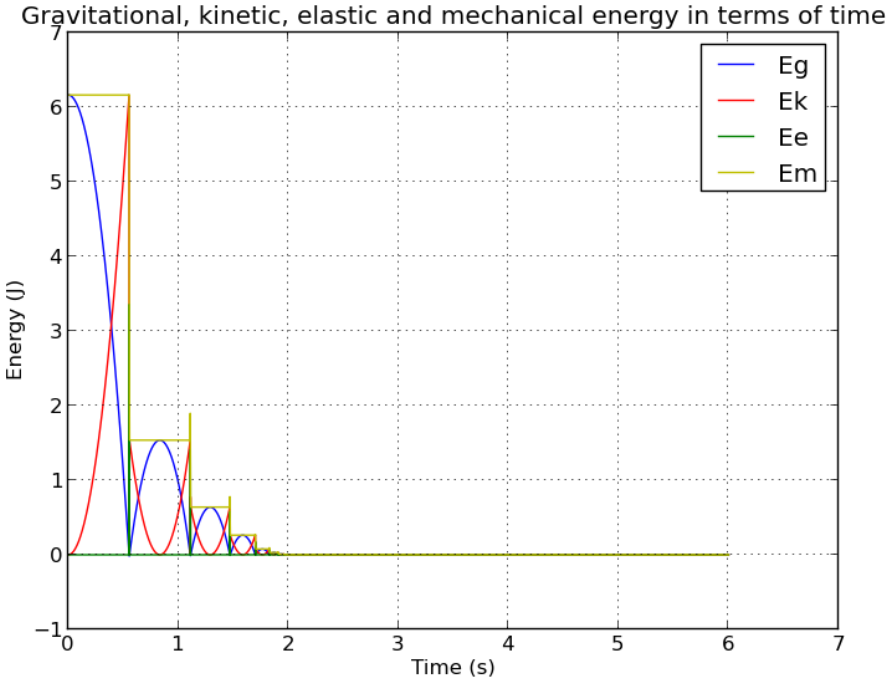

Fig. 27. Energy - time with a restitution coefficient of 0,5.

In the last graph we can see that the damping is working properly by decreasing the energy of the system after every rebound.

For a restitution coefficient of 0,0:

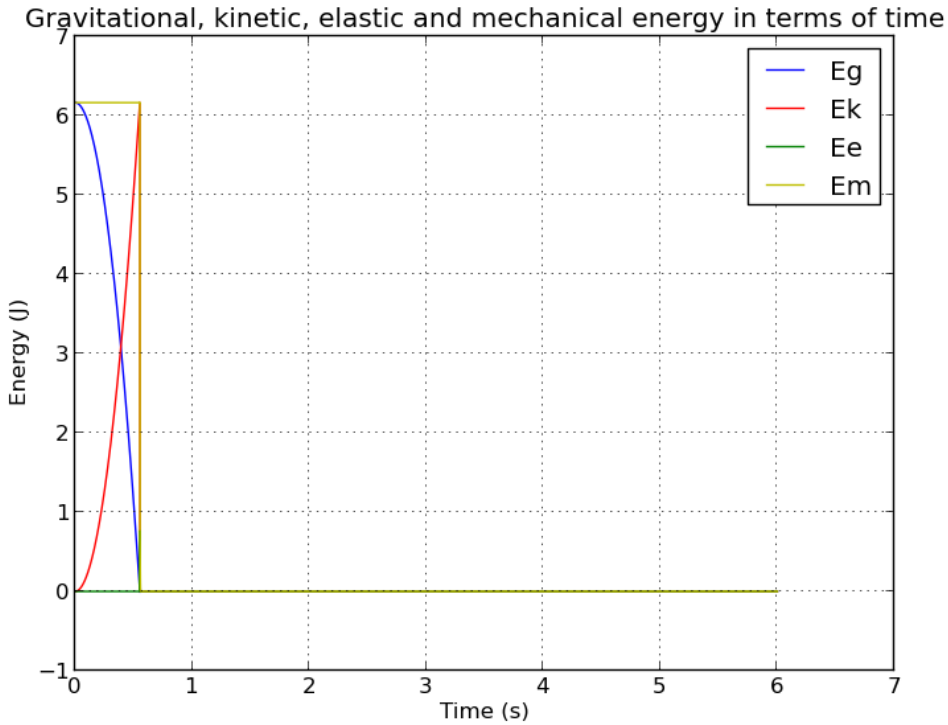

Fig. 28. Energy - time with a restitution coefficient of 0,0.

Finally, with a restitution coefficient of 0, all the energy is lost after the first collision. There is no rebound.

5.3. Effect of the tangential damping

With this last test we wanted to see the performance of the tangential damping force in a simple continuum case.

This experiment consists of a seven-spheres-beam under the gravity force with only an extreme fixed.

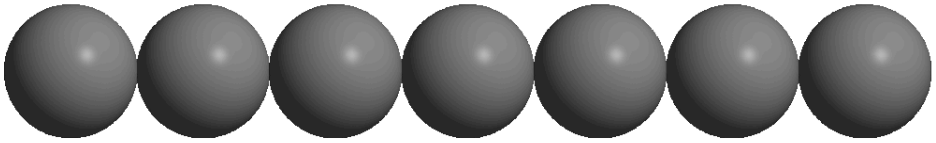

Fig. 29. Initial configuration of the spheres of the beam.

The free spheres start falling due to the gravity force, the tangential spring acts then trying to restore their equilibrium position and so beam starts to vibrate.

The objective of the experiment is to follow the position of the particle at the free extreme and see how the damping works for different values of the restitution coefficient.

The main properties of this test are:

Geometry and Material	
Particle Radius	0,5 $[m]$
Particle Density	100 $[Kg/m^3]$
Young's Modulus	$2{,}1 \cdot 10^7$ $[N/m^2]$
Poisson Ratio	0,2
Problem Data	
DEM simulation	Continuum
Integration Scheme	Forward Euler
Search Step	10
Simulation Time	6 $[s]$
Time Step	0,0001 $[s]$

Table 5. Characteristics of the damping test 3.

In order to see the results clearly, we have represented the evolution of the position of the particle at the free extreme in terms of time for different values of the restitution coefficient.

For a restitution coefficient of 1:

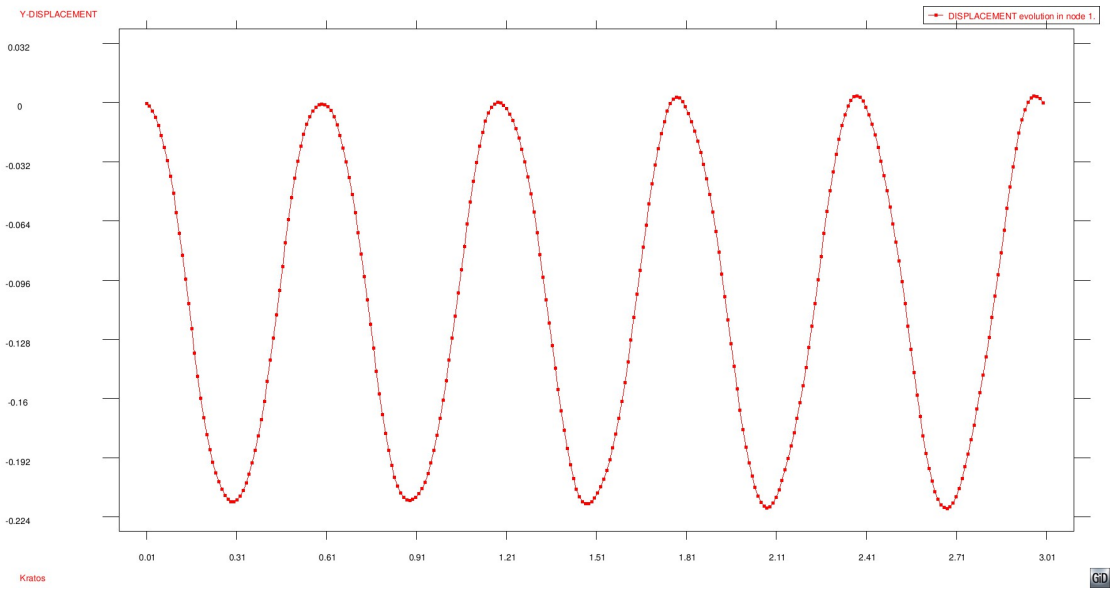

Fig. 30. Position 'Y' in terms of time with a restitution coefficient of 1.

The beam does not stop vibrating for a restitution coefficient of 1, when no damping is applied.

For a restitution coefficient of 0,5:

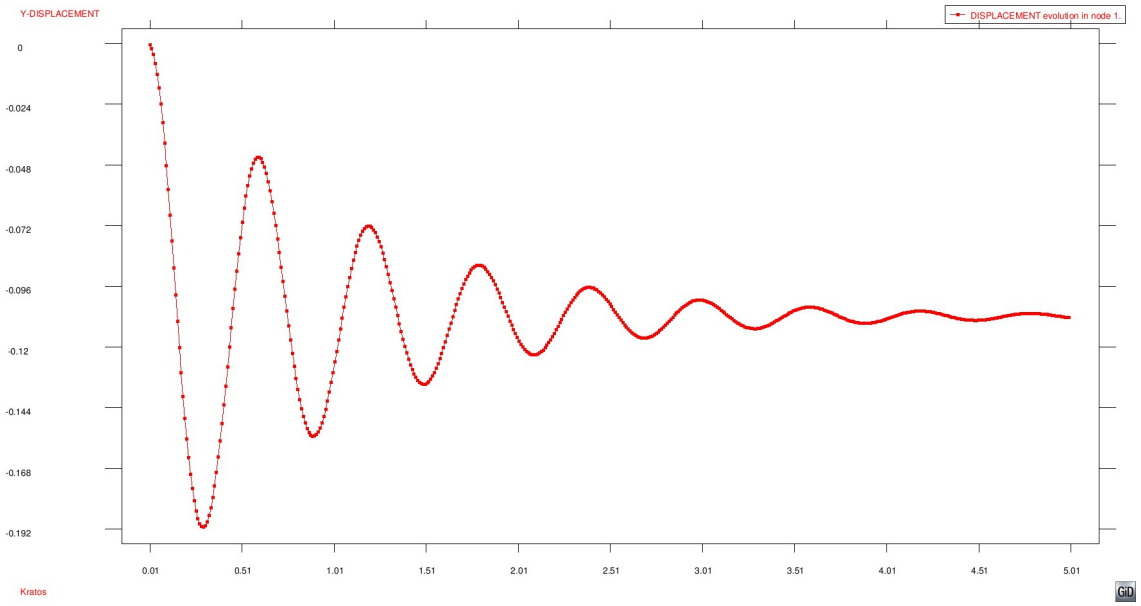

Fig. 31. Position 'Y' in terms of time with a restitution coefficient of 0,5.

The progressive decrease in the amplitude of vibration shows the effect of the tangential damping force.

For a restitution coefficient of 0,0:

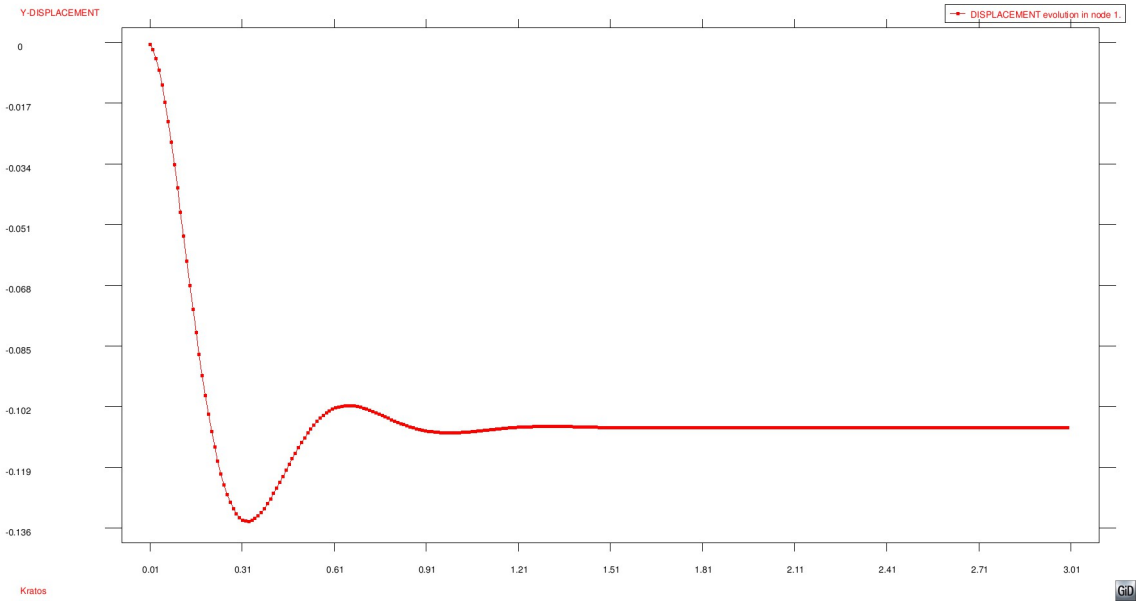

Fig. 32. Position 'Y' in terms of time with a restitution coefficient of 0,0.

With a critical damping the beam stops vibrating after a few time.

This test illustrates the role of the damping force in a continuum simulation. Without it, any continuum system would destabilize and may eventually explode.

6. DEM for discontinuum

As we have already said, the Discrete Element Method has a lot of potential applications in a wide range of subjects. Of all these, probably the most extended one is the simulation of discontinuum.

It is well known that the mechanical behaviour of sands and other granular cohesionless geomaterials is different in important respects from that of other materials, and that this difference is due to the particulate nature of the medium.

As such, the DEM has become accepted and widely used to model the mechanical behaviour and flow of particulate geomaterials. An extension to industrial geomaterial applications has occurred over the past several years with modelling of ball mills, dragline excavators, and material transport using conveyor belts. A largely separate research activity to model powders and materials processing is also ongoing.

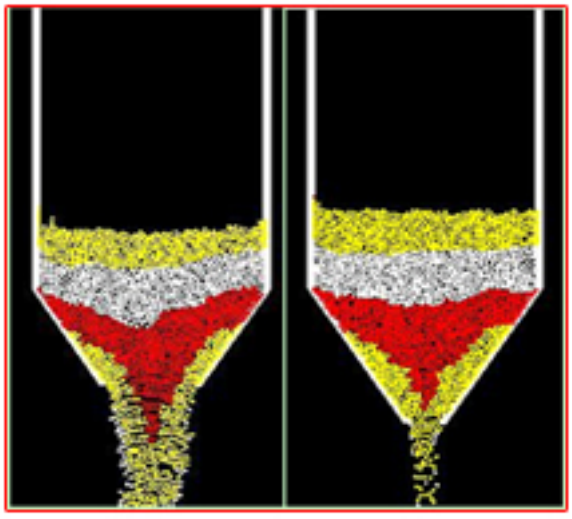

Fig. 33. Flow of particles in a hopper.

This brief chapter will be dedicated to state the bases of the discontinuum simulation that make it different from the continuum, and to show an example performed in CIMNE.

6.1. Technical aspects

Although the most important concepts of the method have already been explained in the *Fundamentals of DEM* chapter, I would like to separately state the unique notion that must be kept in mind when dealing with discontinuum problems.

The basic idea of the discontinuum simulation in DEM is that every particle is an independent entity that interacts with other particles through the linear-spring-dashpot model explained before.

The contact forces originated by this model only appear when there is overlap between two neighbouring particles. When there is no overlap, no forces will appear and so there will be no interaction between two particles. The interaction in discontinuum only takes place when two particles are in contact.

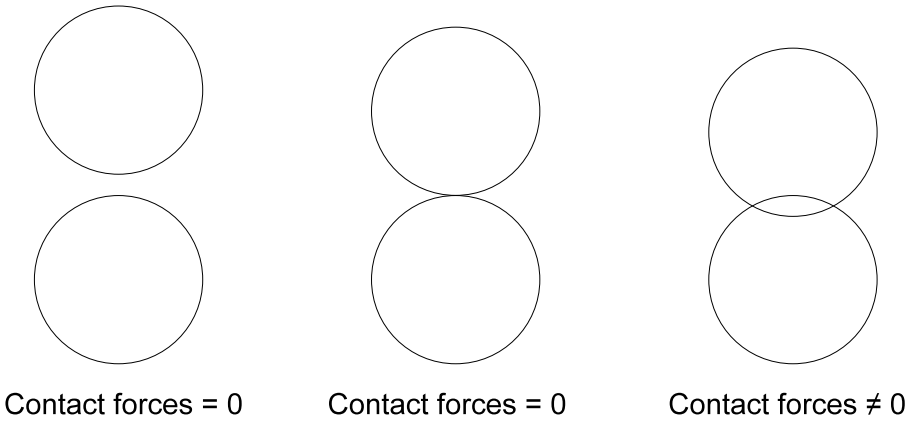

Fig. 34. Interaction between two spheres in discontinuum simulations.

Just as a reminder, the contact forces in the normal direction are computed as:

$$\text{Contact forces} = F_{sn} + F_{dn} = k_n\delta + \eta_n v$$

Where δ is the overlap between the two particles.

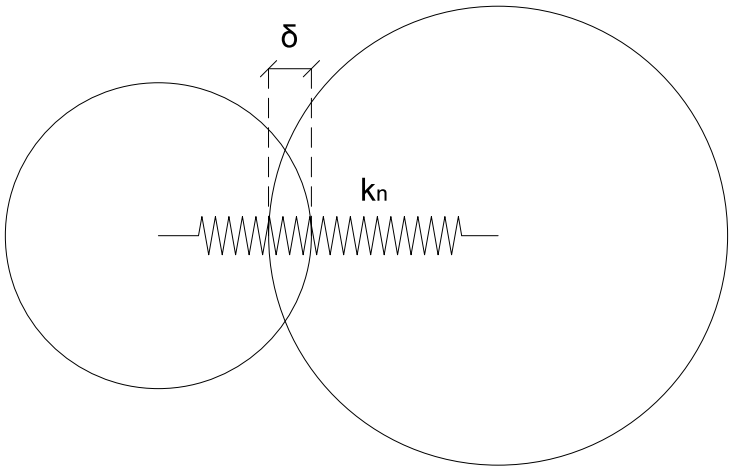

Fig. 35. Overlap or deformation of the linear spring of the contact model.

An additional remark is that, in discontinuum simulations, the tangential damping is not activated so as to avoid excessive energy losses when a sphere is rolling.

6.2. Discontinuum simulation: sand clock

For centuries, a sand hourglass has been a simple common time measuring tool as well as a relatively accurate reliable measure for scientific experiments. Nevertheless, until quite recently, even at the age of supercomputers and efficient numerical methods such as the finite element method, it has not been possible to accurately model this simple phenomenon. A highly varying geometry, and interacting objects were the main obstacles to any efficient approach.

The aim of this example is to perform a discontinuum simulation of DEM with a large number of particles in order to test the effectiveness of the damping force in a more practical case.

Pre-processing

I first designed the geometry of the container for the sand using the CAD of GID.

The main dimensions of the container are the following:

Geometry	
Maximum radius	4 [*cm*]
Minimum radius	0,5 [*cm*]
Height	18 [*cm*]

Table 6. Main measures of the container.

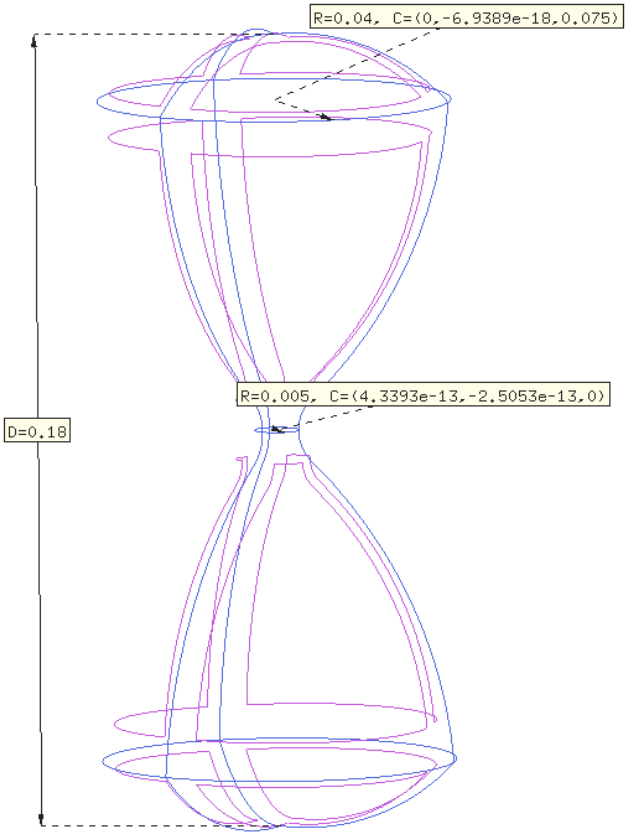

Fig. 36. Geometry of the container. Dimensions in meters.

Since we are simulating discontinuum, before meshing the geometry we had to fix all the particles of the receptacle to make it monolithic.

In addition to this, we defined the properties of the material and the characteristics of the experiment. Both, the sand and the container, were given the same material.

Material	
Particle Density	100 [Kg/m^3] [1]
Young's Modulus	$1 \cdot 10^6$ [N/m^2]
Poisson Ratio	0,2
Dynamic Friction Angle	40^o
Restitution Coefficient	0,0 [2]
Problem Data	
DEM simulation	Discontinuum
Integration Scheme	Forward Euler
Search Step	25
Time Step	$1 \cdot 10^{-4}$ [s]
Simulation Time	20 [s]

Table 7. Properties of the sand clock simulation.

It has been mentioned before, but the DEM Application does not allow creating smooth surfaces. Thereby, in order to mesh the container, we had no choice but to divide the surfaces into finite elements and fill them with uniform spheres at the nodes.

In this example we can clearly see how inconvenience it is. Only to mesh the container for the sand without holes we need over 30.000 spheres. If one looks carefully at the resulting mesh it can be noticed the curious texture of the surfaces, as a result of the accumulation of thousands of spheres.

[1] One should notice that we did not use the real properties of any kind of sand when defining the granular material. This was a means to reduce the computational cost.

[2] For this test and the subsequent experiments we are going to use a restitution coefficient of 0,0 in order to gain stability and thus increase a bit the time step, without having instability problems, making the computation faster.

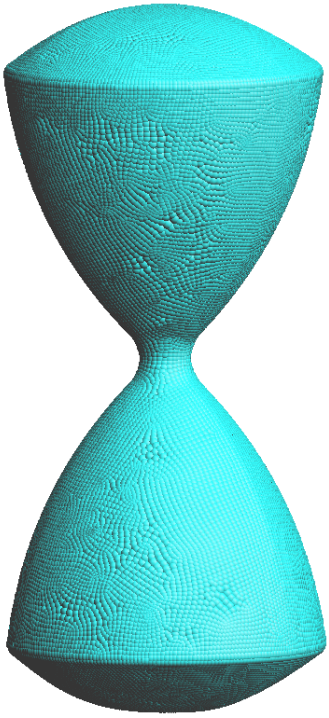

Fig. 37. Mesh of the container.

With respect to the sand, we meshed a spherical volume with a non-uniform distribution of around 40.000 little spheres, and we let it fall from the upper part of the container under the gravity force. The idea was that the group of spheres scattered after getting in contact with the walls of the receptacle, and then fell gradually to its lower part, like in a sand clock.

Fig. 38. Mesh of the sand.

Post-processing and analysis of results

Although it is better to watch the resulting computation in a video, we can have an idea of it by seeing some snapshots.

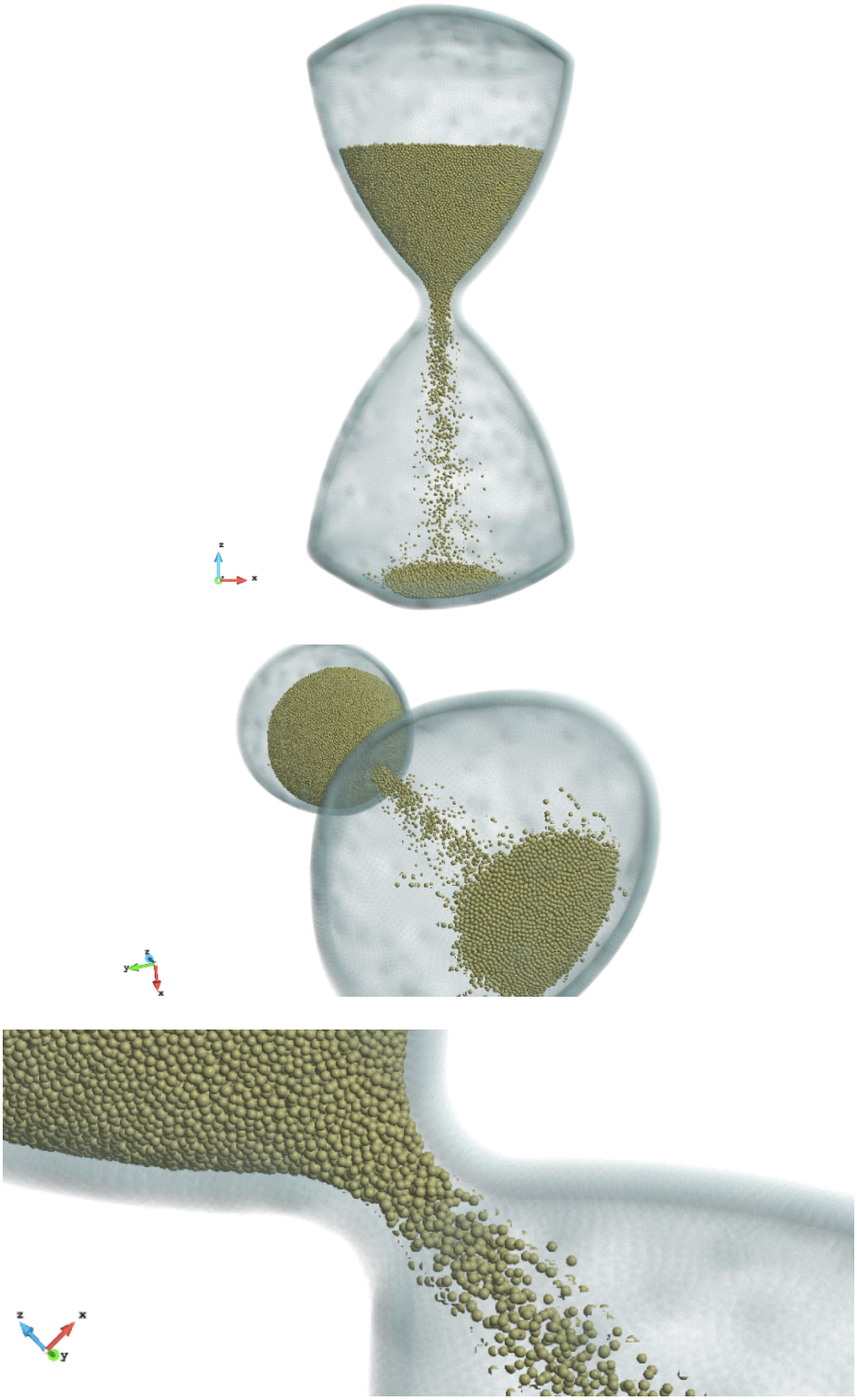

Fig. 39. Screenshots of the resulting video.

From the resulting video, we have verified that the damping force works properly, making the spheres bounce with almost no rebound, and that DEM simulations of granular material are perfectly valid.

However, one thing that needs improvement is the computational cost of these kinds of simulations. For instance, only to run this simple case, various days of calculation were needed.

As it has been mentioned above, one can carefully choose the properties of the material so that the problem runs faster, but it is not a good practice if we aim to simulate real materials. Another possibility could be to rewrite the code in order to make it more computationally efficient. However, it would not probably mean a great change.

In this regard, for the Discrete Element Method to be competitive against other methods, parallelization of the main processes in the computational scheme must play a crucial role in reducing the total calculation time. In fact, it is currently being implemented in the code used in CIMNE and, without going into the details; some basic concepts of this matter are presented in the last chapter of this work.

7. DEM for continuum

We have already seen an example of the most widely known application of the Discrete Element Method, the discontinuum. In this chapter we are going one step further to simulate continuum cases.

The fracture behaviour of solids such as concrete, rock, ceramics, and other brittle materials under severe loading has become an area of increased research in recent years. These materials are complex and extremely heterogeneous, especially after they degrade from solid to particulate. Reproducing the behaviour exhibited by these materials with continuum methods requires complex constitutive models containing a large number of parameters and/or internal variables, such as yield surfaces and equation of state descriptors.

The discrete element method has proven to be a powerful and versatile numerical tool for modelling the behaviour of granular and particulate systems, and also for studying the micromechanics of materials such as soil at the particle level. However, the method also has the potential to be an effective tool to model continuum problems (i.e. solids), especially those that are characterized by a transformation from a continuum to a discontinuum. Such problems include failure of concrete structures, fragmentation of rock due to blasting, and fracture of ceramics and other quasi-brittle materials under high velocity impact.

Continuum based methods such as the finite element method are challenging to apply to these problems and are plagued by the need for continuum constitutive models, severe element distortion, and frequent re-meshing. In contrast, DEM has the capability to capture the complicated behaviour of actual materials by using a discretization scheme that is simple in concept and implementation.

In this chapter, we first are going to expose the technical aspects that differentiate continuum simulation from discontinuum, and afterwards we will see some tests performed with DEM simulation.

7.1. Technical aspects

As we have said before, the main differences between simulation of continuum and discontinuum are in the definition of the forces of the linear-spring-dashpot contact model.

Differently from discontinuum, any continuum contact between two neighbouring particles must be understood as a spring linking their centres that is in equilibrium when the two particles are tangentially in contact. Thereby, as they get closer the spring will be shortened and so repulsive forces will appear. On the other hand, if they get farther the attraction forces of the spring will keep them together. Furthermore, the damping force will always be acting as long as the contact has not failed.

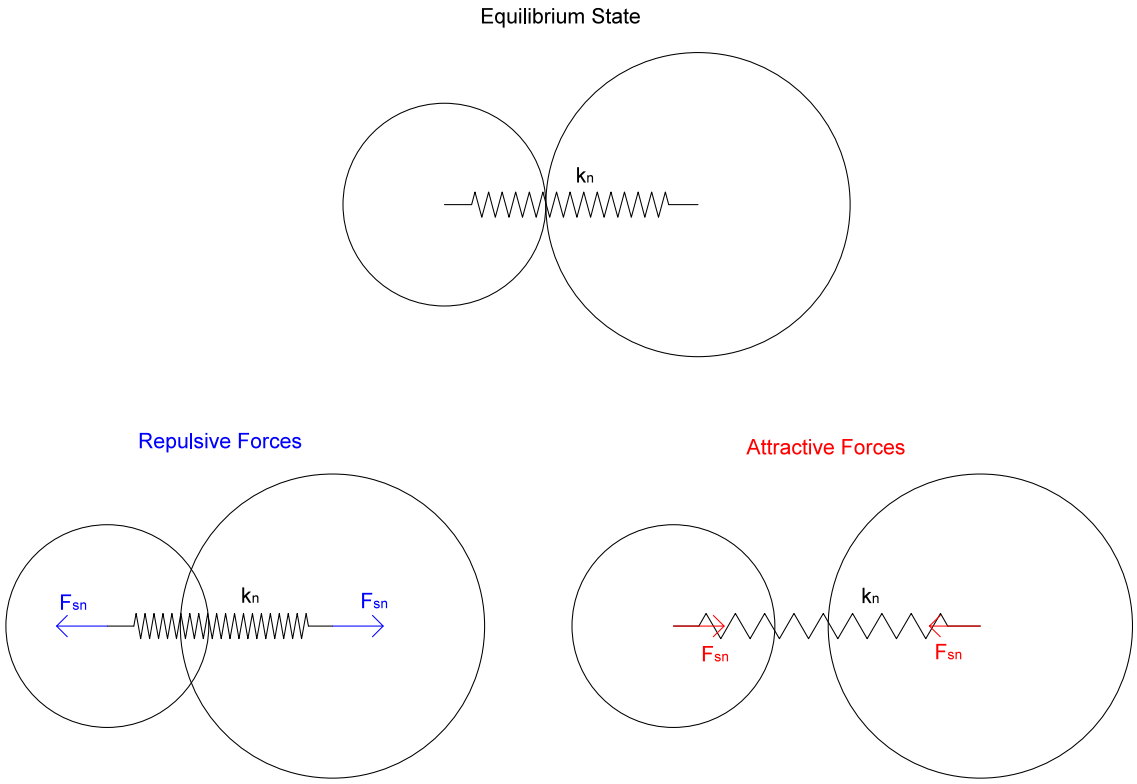

Fig. 40. Scheme of the interaction of particles in continuum simulations.

This contact, however, may not always work like this. Depending on the forces acting on the particles and their corresponding displacements, any continuum contact will fail if some conditions are exceeded. These conditions depend on the failure criterion specified by the user.

Once the contact fails, the two neighbouring particles interact in the same way as in discontinuum, and so from that moment onwards, only when there is overlap between them, contact forces will appear.

With regard to the stiffness coefficient, we have already said that its value is different from the discontinuum one because it is multiplied by a coefficient that affects the contact area. In the following lines, we will explain what this coefficient means and how it is computed.

7.1.1. Corrected contact area method

As it has been stated in the *Fundamentals of DEM* chapter, for discontinuum simulations we compute the contact area A between two neighbouring spheres as follows.

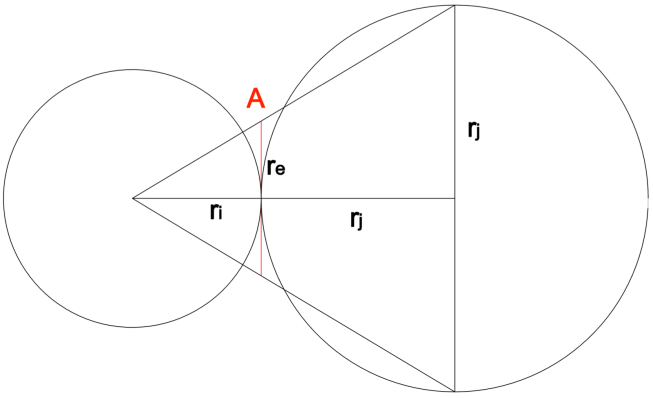

Fig. 41. Considered contact area in discontinuum simulations.

$$r_e = \frac{r_i r_j}{r_i + r_j}$$

$$A = \pi r_e^2 = \pi \left(\frac{r_i r_j}{r_i + r_j} \right)^2$$

In continuum cases, however, this formula would lead to errors in the computation of the forces and thus must be corrected.

Just as a reminder, in discontinuum, the spring force in the normal direction is computed as:

$$F_{sn} = k_n \Delta L$$

Where ΔL is the deformation of the spring, and k_n is the normal stiffness, which depends on the contact area A:

$$k_n = \frac{EA}{L_0}$$

When computing the forces applied on a spherical particle of any DEM simulation, we take into account the contribution of each neighbour through a loop. For an independent entity, like in discontinuum, the total force can be computed without important errors. Nevertheless, when a particle is surrounded by a lot of neighbours, like in continuum simulations, the total force computed with the contact area formula stated before would be wrong due to the overlap of contact areas between the different neighbours.

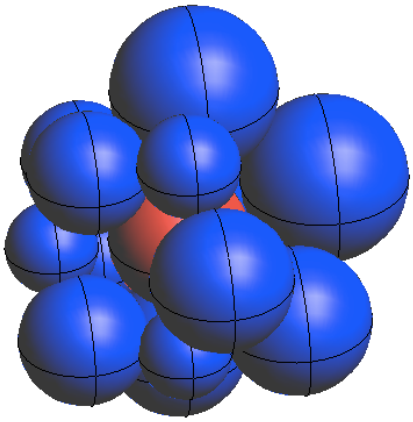

Fig. 42. Particle in red surrounded by blue neighbours.

Therefore, in order to reduce this overlap of areas, we must multiply the contact area formula by a corrector coefficient.

The idea behind this corrector coefficient is to reduce the contact area of each neighbour by considering that the sum of all the neighbouring contact areas should be similar to the surface area of a convex regular polyhedron with as many faces as neighbours.

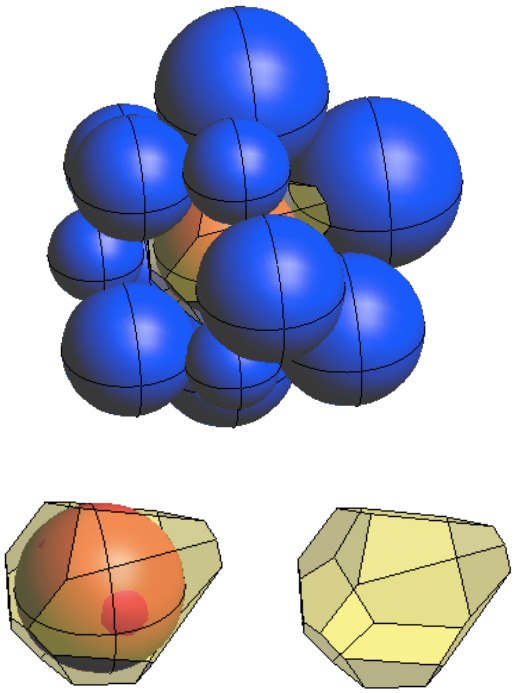

Fig. 43. Polyhedron associated to a particle.

However, it is common knowledge that there are only five different convex regular polyhedra, called the Platonic Solids: tetrahedron (4 faces), hexahedron (6 faces), octahedron (8 faces), dodecahedron (12 faces) and icosahedron (20 faces).

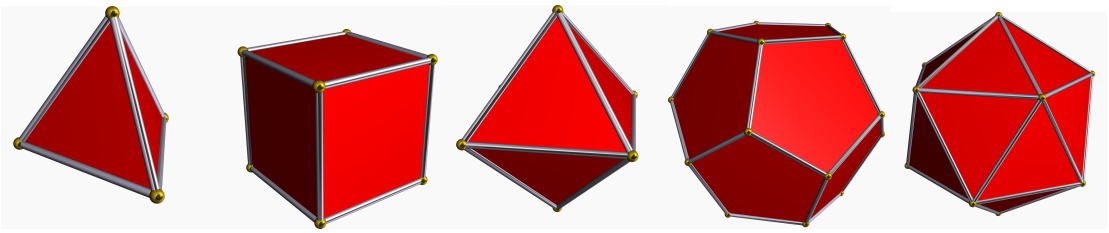

Fig. 44. Platonic solids.

Since every particle can have any number of neighbours, we need to use the surface area of a fictitious regular convex polyhedron with any number of faces. In order to do so, we interpolate from the already known surface area of the five Platonic solids.

That being said, for each particle i with a number of neighbours n, we compute the corrector coefficient α as:

$$\alpha_i = R_{a,n} \frac{\text{Surface Area of the Particle}}{\text{Total Contact Area}} = R_{a,n} \frac{4\pi r_i^2}{\sum_{j=1}^{n} \pi \left(\frac{r_i r_j}{r_i + r_j} \right)^2} \qquad \text{(Eq. 32)}$$

Where $R_{a,n}$ is the ratio between the surface area $A_{s,n}$ of the fictitious regular convex polyhedron of n faces and the area of the sphere inscribed.

$$R_{a,n} = \frac{A_{s,n}}{4\pi r_i^2} \qquad \text{(Eq. 33)}$$

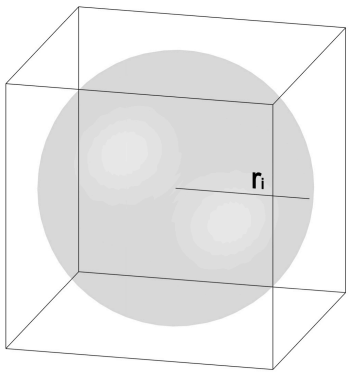

Fig. 45. Sphere inscribed in a hexahedron.

If we substitute $R_{a,n}$ in the expression of α_i, it is easier to understand the meaning of the corrector coefficient:

$$\alpha_i = \frac{A_{s,n}}{4\pi r_i^2} \frac{4\pi r_i^2}{\sum_{j=1}^{n} \pi \left(\frac{r_i r_j}{r_i + r_j} \right)^2} = \frac{A_{s,n}}{\sum_{j=1}^{n} \pi \left(\frac{r_i r_j}{r_i + r_j} \right)^2} \qquad \text{(Eq. 34)}$$

This way, one can see that this coefficient represents how different is the total contact area with respect to the area of the fictitious polyhedron. Due to the overlap of contact areas between the different neighbours, the total contact area will always be larger than the area of the polyhedron and so α_i will take any value

between 0 and 1 ($0 < \alpha_i < 1$).

Therefore, in order to find out the corrector coefficient, we first must compute the ratio $R_{a,n}$ for the five Platonic solids.

Number of neighbours (n)	Regular Convex Polyhedron	Surface Area ($A_{s,n}$)	Ratio of Areas ($R_{a,n}$)
4	Tetrahedron	$24r_i^2\sqrt{3}$	$\frac{6\sqrt{3}}{\pi} \simeq 3{,}308$
6	Hexahedron	$24r_i^2$	$\frac{6}{\pi} \simeq 1{,}910$
8	Octahedron	$12r_i^2\sqrt{3}$	$\frac{3\sqrt{3}}{\pi} \simeq 1{,}654$
12	Dodecahedron	$\frac{600r_i^2}{25+11\sqrt{5}}\sqrt{\frac{5+2\sqrt{5}}{5}}$	$\frac{150}{\pi(25+11\sqrt{5})}\sqrt{\frac{5+2\sqrt{5}}{5}} \simeq 1{,}325$
20	Icosahedron	$\frac{120r_i^2\sqrt{3}}{7+3\sqrt{5}}$	$\frac{30\sqrt{3}}{\pi(7+3\sqrt{5})} \simeq 1{,}207$

Table 8. Ratio of surface areas $R_{a,n}$ for each platonic solid.

Then we interpolate from these five values to obtain the ratios for different numbers of neighbours.

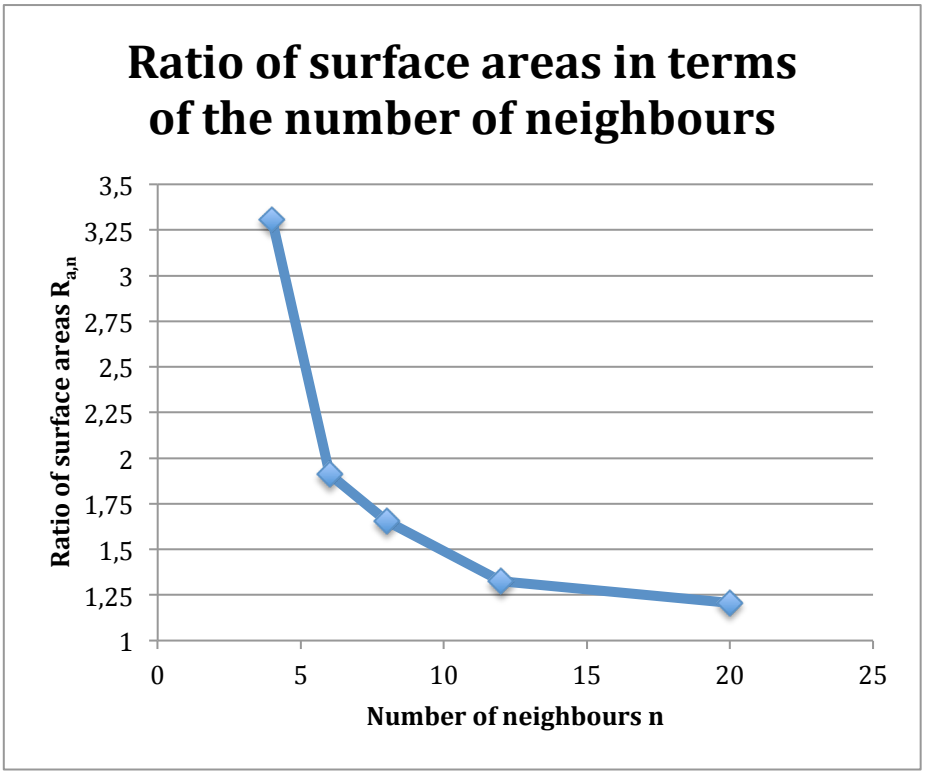

Fig. 46. Ratio of surface areas $R_{a,n}$ in terms of the number of neighbours.

As the number of neighbour increases, the surface area of the fictitious polyhedron becomes more similar to that of the sphere inscribed, and so the ratio gets closer to 1. Obviously, it is not needed the ratio for less than 4 neighbours because there would be no problems of area overlap with such a small number of neighbours. Furthermore, for more than 20 neighbours, we have simply considered a constant ratio of 1,15 because, unless the mesh quality is so poor that we have important deviations in the radius of the particles, it is almost impossible to be in such a case. In fact, in a 3D analysis, the average number of neighbours is around 11.

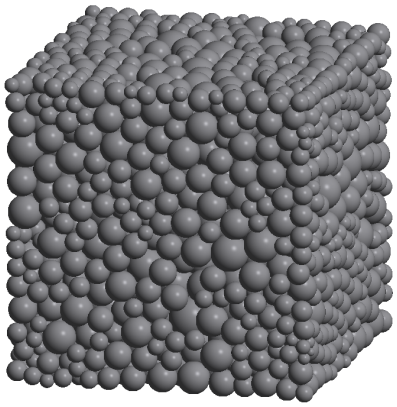

Fig. 47. Cube meshed with a non-uniform distribution of spheres.

As we can see in figure 47, although the mesh has a non-uniform distribution of spheres, the radiuses of the particles are quite alike and thus there will not be particles with more than 20 neighbours.

On balance, we have seen that the parameter α is a corrector coefficient applied to the contact area formula in order to minimize the error in the computation of the local forces derived from the overlap of the neighbouring contact areas. This coefficient is computed for each particle and its value depends on the number of neighbours.

If we now think of a solid body composed by a certain number of spherical particles, like in continuum simulations, we may clearly differentiate two kinds of particles in such case: the particles on the boundary of the solid, and the particles inside that boundary.

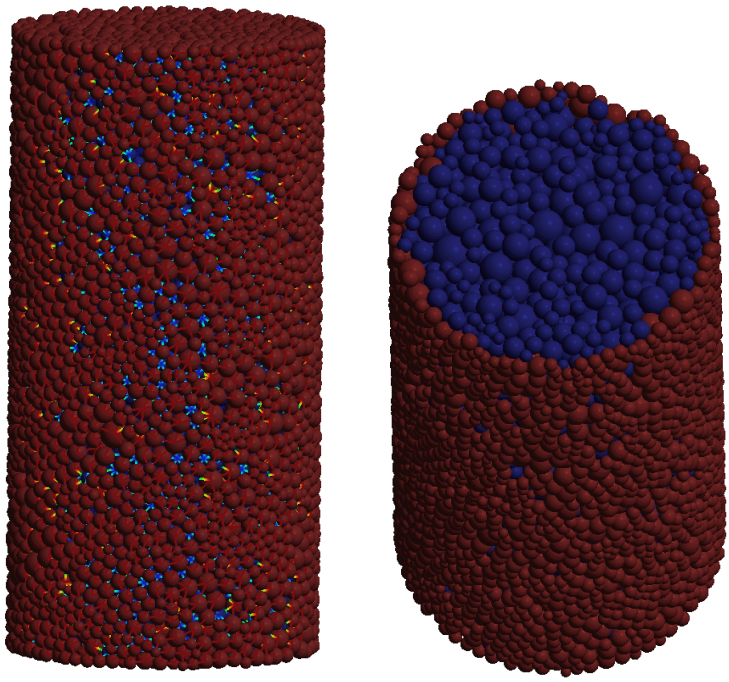

Fig. 48. The particles in red are the so-called skin spheres.

As one can see from the picture, the particles inside the boundaries of the specimen are completely surrounded by neighbouring spheres, whereas the particles on the boundaries are just partially surrounded.

Therefore, it seems illogical to correct the contact area formula through the same criterion for both kinds of particles.

It is for this reason that, before any computations, the spheres on the boundary of any solid body are defined as skin particles, differently from the ones inside the contour.

Thereby, for the particles inside the boundary we compute the corrector coefficient α as we have already stated before:

$$\alpha_i = R_{a,n}\frac{\text{Surface Area of the Particle}}{\text{Total Contact Area}} = R_{a,n}\frac{4\pi r_i^2}{\sum_{j=1}^{n}\pi\left(\frac{r_i r_j}{r_i + r_j}\right)^2}$$

And, on the other hand, to compute α for the particles on the boundary we consider that any skin sphere is totally surrounded by 11 neighbours, like an average interior particle, and then we reduce the ratio of areas so as to take into account that it is only partially surrounded.

$$\alpha_{i,skin} = \frac{n}{11}R_{a,11}\frac{\text{Surface Area of the Particle}}{\text{Total Contact Area}} = \frac{n}{11}R_{a,11}\frac{4\pi r_i^2}{\sum_{j=1}^{n}\pi\left(\frac{r_i r_j}{r_i + r_j}\right)^2} \qquad \text{(Eq. 35)}$$

Where n is the number of neighbours (n < 11).

7.1.2. Failure criterion

So far we have thoroughly seen one of the most important differences between discontinuum and continuum simulations, the definition of the contact forces. Nonetheless, there is another differential characteristic of continuum that must be explained, the failure criterion.

We have mentioned before that any continuum contact will eventually fail if some conditions are exceeded. These conditions conform the failure criterion that must be defined by the user.

For the moment, two different failure criteria have been implemented for continuum simulations of DEM Application: an adaptation of the 2D Mohr-Coulomb failure criterion, and an uncoupled criterion.

7.1.2.1. 2D Mohr-Coulomb criterion

Mohr-Coulomb is a failure criterion especially adequate for frictional materials such as concrete, rocks and soil.

The basis of this criterion is to compare the stress state of any contact with the characteristic failure line of the simulated material in order to assess whether it fails or not.

To obtain the failure line of the material we first need to know its interior friction angle and its cohesion parameter. In case we do not know them, they can be deduced from the tensile and compression strength of the material.

Consider the following scheme and let ϕ be the interior friction angle of the material, c its cohesion parameter, σ_{tmax} its tensile strength and σ_{cmax} its compression strength. Compressive stresses have been considered positive.

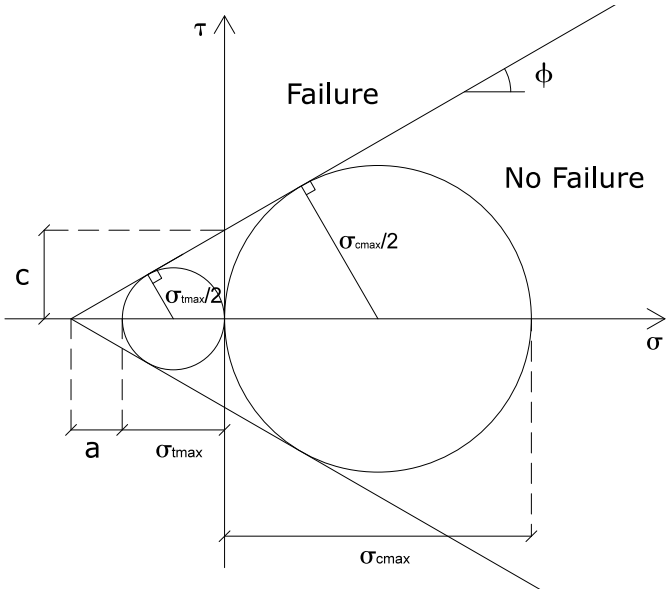

Fig. 49. Mohr-Coulomb failure criterion.

One can obtain c and tanϕ in terms of σ_{tmax} and σ_{cmax} through some simple steps:

Looking at the triangles in figure 49 one can deduce that:

$$\sin\phi = \frac{\sigma_{tmax}/2}{a+\sigma_{tmax}/2} \rightarrow a = \frac{\sigma_{tmax}/2}{\sin\phi} - \frac{\sigma_{tmax}}{2}$$

$$\sin\phi = \frac{\sigma_{cmax}/2}{a+\sigma_{tmax}+\sigma_{cmax}/2} \rightarrow a = \frac{\sigma_{cmax}/2}{\sin\phi} - \sigma_{tmax} - \frac{\sigma_{cmax}}{2}$$

Imposing equality:

$$a = a \rightarrow \frac{\sigma_{tmax}/2}{\sin\phi} - \frac{\sigma_{tmax}}{2} = \frac{\sigma_{cmax}/2}{\sin\phi} - \sigma_{tmax} - \frac{\sigma_{cmax}}{2} \rightarrow \sin\phi = \frac{\sigma_{cmax}-\sigma_{tmax}}{\sigma_{cmax}+\sigma_{tmax}}$$

$$\sin\phi = \sin\phi \rightarrow \frac{\sigma_{tmax}/2}{a+\sigma_{tmax}/2} = \frac{\sigma_{cmax}/2}{a+\sigma_{tmax}+\sigma_{cmax}/2} \rightarrow a = \frac{\sigma_{tmax}^2}{\sigma_{cmax}-\sigma_{tmax}}$$

Through a trigonometric relation, we find tanϕ:

$$\tan\phi = \frac{\sin\phi}{\sqrt{1-\sin^2\phi}} = \frac{\sigma_{cmax}-\sigma_{tmax}}{2\sqrt{\sigma_{cmax}\sigma_{tmax}}} \qquad \text{(Eq. 36)}$$

Furthermore, taking into account that $\tan\phi = \frac{c}{a+\sigma_{tmax}}$, we get the cohesion c:

$$c = \frac{\sqrt{\sigma_{cmax}\sigma_{tmax}}}{2} \qquad \text{(Eq. 37)}$$

That being said, let us explain how we obtain the stress state at any contact point.

Due to the nature of the contact model used in the DEM, with linear-spring-dashpot systems in the local normal direction and in the two tangential, we consider the contact between two neighbouring particles as a plane with only one normal stress following the local normal direction between the spheres, and shear stresses surrounding the plane. We assume that the normal stress in the other direction of the plane is null.

Thereby, at every time step, we may only have two different stress states: one with compressive stresses and another with tensile stresses.

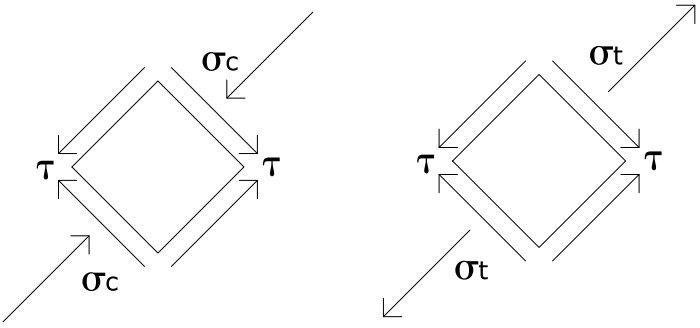

Fig. 50. Possible stress states.

The normal stress is obtained from the division of the local normal force, F_n, by the corrected contact area, A.

$$\sigma_i = \frac{F_n}{A} \qquad \text{(Eq. 38)}$$

where i ={ c , t }

On the other hand, to compute the shear stress, we first calculate the norm of the vectorial sum of the two local tangential forces and then we divide it by the same contact area.

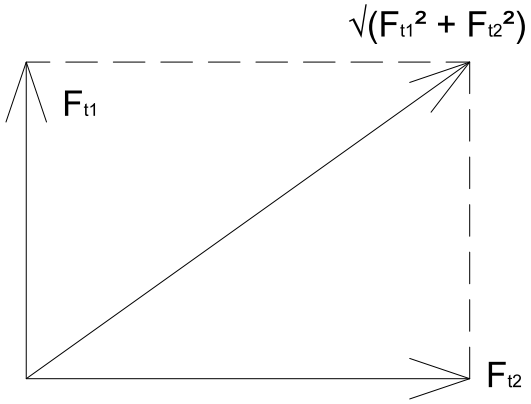

Fig. 51. Vectorial sum of the two tangential forces.

$$\tau = \frac{F_t}{A} = \frac{\sqrt{F_{t1}^2 + F_{t2}^2}}{A} \qquad \text{(Eq. 39)}$$

These stresses, both the normal and the tangential, can be represented with a Mohr-Coulomb diagram to obtain the stress state at any particular contact and time step.

Thereby, we can draw the Mohr circumference for any of the two possible stress states as well as the failure line of the material in order to verify whether the contact has failed or not.

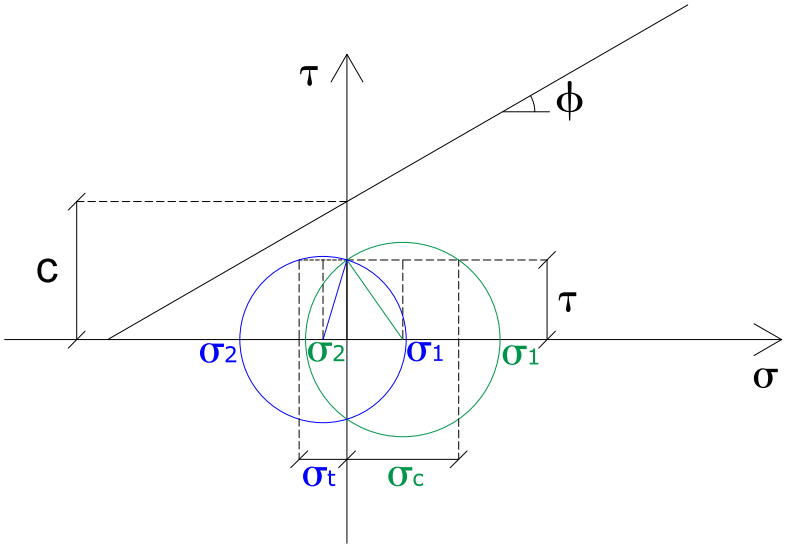

Fig. 52. Mohr-Coulomb diagram for the two possible stress states.

We must first calculate the principal stresses of our particular stress state in order to compare it with the failure line.

$$\sigma_1 = \frac{\sigma_i}{2} + \sqrt{\left(\frac{\sigma_i}{2}\right)^2 + \tau^2} \quad \text{(Eq. 40)}$$

$$\sigma_2 = \frac{\sigma_i}{2} - \sqrt{\left(\frac{\sigma_i}{2}\right)^2 + \tau^2} \quad \text{(Eq. 41)}$$

where i ={ c , t }

In a generic failure state we have:

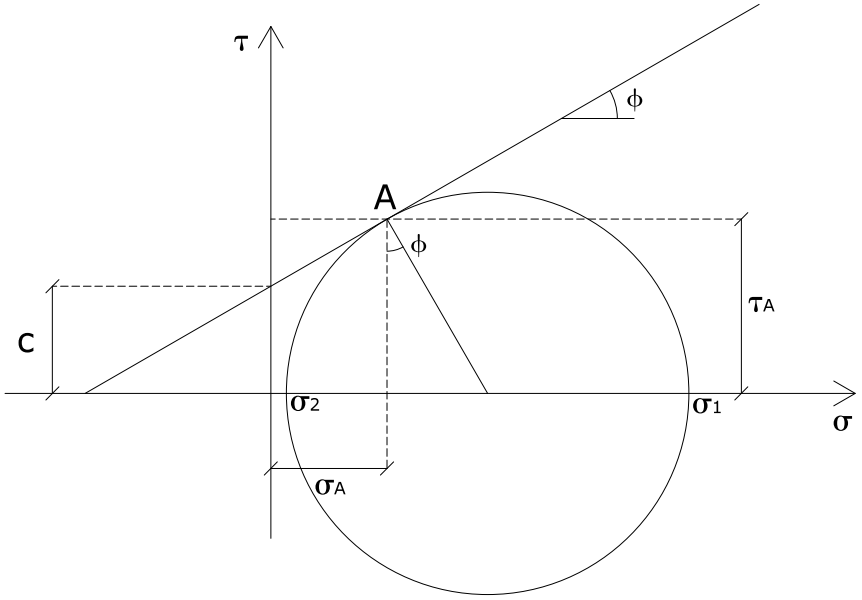

Fig. 53. Mohr circumference in a generic failure state.

The shear stress at a failure state can be written as:

$$\tau_A = c + \sigma_A \tan\phi \qquad \text{(Eq. 42)}$$

And so when $\tau_A \geq c + \sigma_A \tan\phi$, the contact fails.

If we rewrite the last equation in terms of σ_1 and σ_2, we have:

$$\frac{\sigma_1-\sigma_2}{2}\cos\phi \geq c + \left[\frac{\sigma_1+\sigma_2}{2} - \frac{\sigma_1-\sigma_2}{2}\sin\phi\right]\tan\phi \qquad \text{(Eq. 43)}$$

Multiplying the whole equation by $\cos\phi$ and rearranging terms we finally obtain the failure condition:

$$\sigma_1 - \sigma_2 \geq 2c\cos\phi + (\sigma_1 + \sigma_2)\sin\phi \qquad \text{(Eq. 44)}$$

This 2D Mohr-Coulomb criterion is just a provisional method that allows us to define the failure at the contacts of every particle. In the near future, we hope to introduce a 3D Mohr-Coulomb failure criterion that could represent the global failure of the continuum, taking into account factors like the confinement, apart from the local forces of every contact. The main obstacle is that we first need to think of a way to compute the 3D stress tensor of every particle, which is not a trivial process. Some authors have developed approximated methods to calculate this stress tensor [13, 14, 15].

7.1.2.2. Uncoupled criterion

Just like in the previous case, this criterion permits to define the failure at the contacts of the particles, but it is not a global failure criterion.

In this case, the method to determine the failure of any contact is simpler than the previous one.

We first compute a normal stress from the local normal force and the corrected contact area, like in the previous case. Depending on the sign of the force, we will obtain a compressive stress or a tensile stress.

$$\sigma_i = \frac{F_n}{A} \qquad \text{with } i = \{ c , t \}$$

We also calculate a shear stress from the two local tangential forces.

$$\tau = \frac{F_t}{A} = \frac{\sqrt{F_{t1}^2 + F_{t2}^2}}{A}$$

At this point, we no longer represent the stress state with a Mohr-Coulomb diagram. Instead, we just compare these two stresses with some limits. Theses limits are prescribed by the user and depend on the sign of the normal stress computed before.

Thereby, when a contact is under a compression state, the line of the Mohr-Coulomb criterion will determine its failure, and when it is under a tensile state, the criterion applied will be an uncoupled method.

When we say that the criterion applied in the tensile range is an uncoupled method, we mean that any contact under a tensile state can fail either because the normal tensile stress exceeds a certain threshold, or because the shear stress is larger than a maximum value. Both limits depend on the material and must be defined by the user.

Let us introduce a maximum shear stress, τ_{tmax}, a maximum tensile stress, σ_{tmax} and, again, the internal friction angle of the material, ϕ. Then, considering compressions positive, the failure line of the uncoupled criterion can be completely defined as in the figure below.

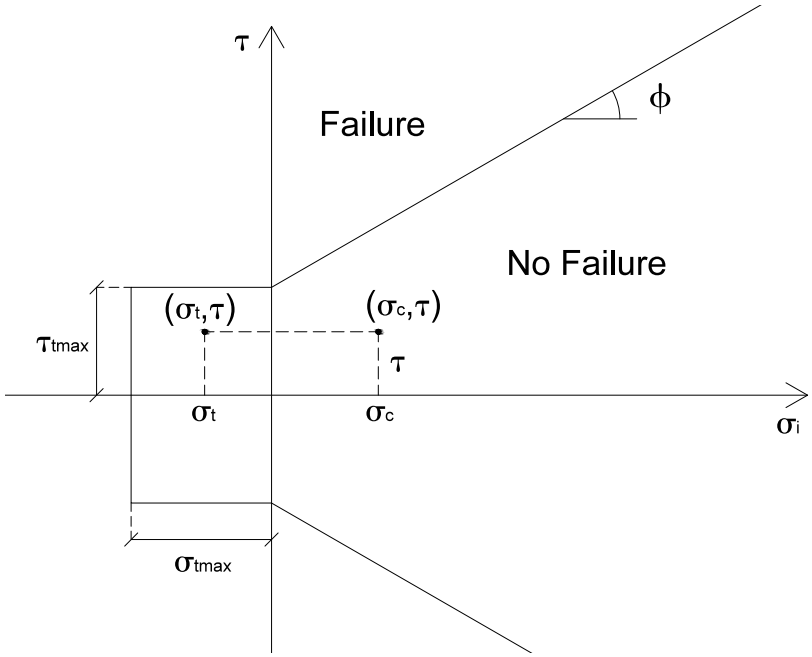

Fig. 54. Uncoupled Criterion.

As one can see, we compute the pair (σ_i , τ) for each contact between two neighbouring particles and verify whether it is inside the limits or not.

Therefore, for $\sigma_i < 0$, any contact will eventually fail either when $\sigma_t > \sigma_{tmax}$ or when $\tau > \tau_{tmax}$.

On the other hand, for $\sigma_i > 0$, the contact will fail when $\tau > \tau_{tmax} + \sigma_c \cdot \tan\phi$.

7.1.3. Brittle - ductile fracture

The two failure criteria presented in this work can only reproduce brittle fracture. This means that, since any contact fails when a prefixed value is exceeded, the continuum simulation will eventually fail with little or no deformation.

These models of fracture are good enough for brittle materials like glass or cast iron. Nevertheless, ductile materials such as steel or aluminium, which fail after large deformations, need damage and plasticity models to represent accurately the fracture. These models should ensure that the fracture energy of the material is conserved over time.

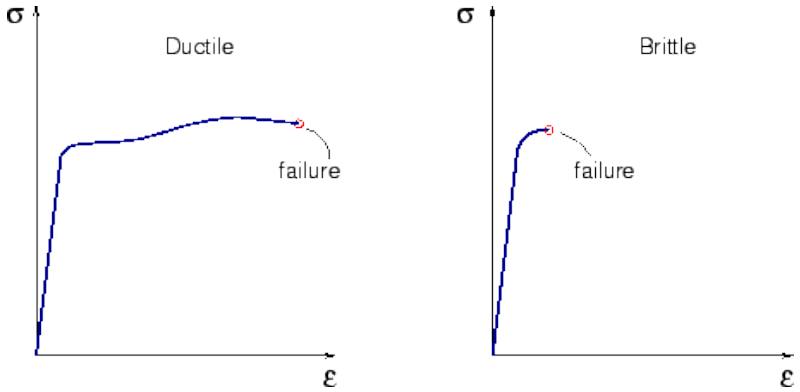

Fig. 55. Ductile failure and brittle failure.

In the intermediate case of concrete or mortars the fracture neither is completely brittle nor perfectly ductile. In this case, a proper simulation of the fracture processes requires the inclusion of the fracture energy.

7.2. Continuum simulations

This chapter will be dedicated to expose a series of experiments aimed to the validation of the application of the discrete element method in continuum cases. The idea is to simulate laboratory tests that are very common in the field of civil engineering using the DEM application. For each one of these tests, we are going to state a brief introduction, explain how they were performed, and show the results and conclusions.

7.2.1. Uniaxial Compression Strength Test

7.2.1.1. Introduction

The Uniaxial Compression Strength test (UCS test) is the most widely used experiment to measure the compressive strength of concrete specimen.

A cylindrical test tube is loaded axially up to failure and the maximum load, F_{max}, is measured in order to compute the compressive strength, f_c:

$$f_c = \frac{F_{max}}{A_c} \qquad \text{(Eq. 45)}$$

Where A_c is the cross-sectional area of the specimen.

Fig. 56. Failure of a test tube in a UCS test.

Under pure uniaxial compression loading, the failure cracks generated are approximately parallel to the direction of applied load with some cracks formed at an angle to the applied load.

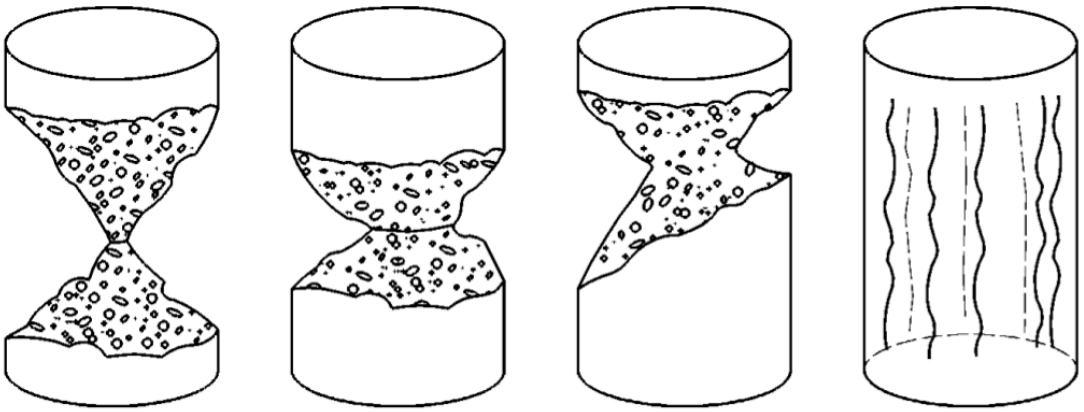

Fig. 57. Possible failure modes after an UCS test.

7.2.1.2. DEM simulation

The main objective of this first test is to break a concrete specimen under a uniaxial load in order to validate its compressive strength and its Young's modulus.

Thereby, we aimed to compare these parameters of the simulated concrete with those of the UPC specimen, with a compressive strength of 32,8 MPa, and a Young's modulus of 24 GPa.

Pre-processing

Using the tools of GID, I first sketched a cylindrical test tube with a diameter of 15

cm and a height of 30 cm. The dark blue represents lines entities, the pink is the colour of surfaces, and the light blue encloses the volume.

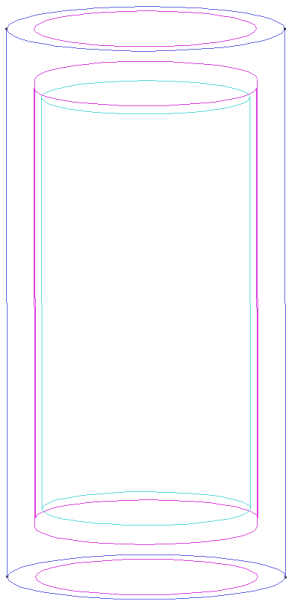

Fig. 58. Geometry of the specimen for the UCS test.

Before meshing it, we defined the properties of the material and the characteristics of the experiment.

Material	
Particle Density	2.500 [Kg/m^3]
Young's Modulus	24 [GPa] [3]
Poisson Ratio	0,2
Dynamic Friction Angle	40º
Restitution Coefficient	0,0
Problem Data	
DEM simulation	Continuum
Integration Scheme	Forward Euler
Search Step	150
Time Step	$5 \cdot 10^{-8}$ [s] [4]
Simulation Time	0,005 [s]
Failure criterion	Uncoupled
τ_{tmax}	8,5 [MPa] [5]
σ_{tmax}	3,3 [MPa]
Internal Friction Angle, ϕ	26,6 °

Table 9. Characteristics of the UCS test.

[3] This is the value of the Young's modulus applied at the contacts in the particulate level. It is not necessarily the same as the global Young's modulus of the specimen we are trying to model.

[4] The time step used in each test is the maximum one that has not instability problems.

[5] The values of the failure parameters were chosen after various attempts trying to simulate properly the behaviour of this concrete.

Then we meshed it with a non-uniform distribution of over 10.500 spheres.

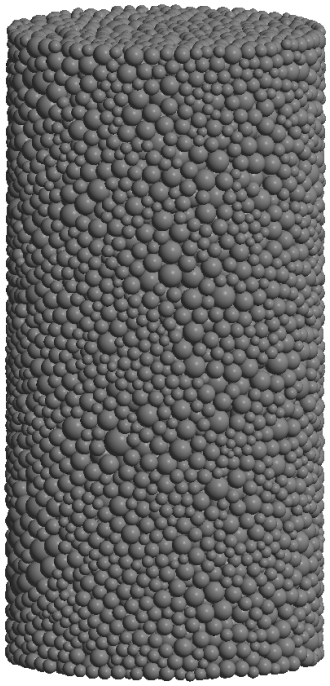

Fig. 59. Mesh of the specimen for the UCS test.

At this point, in order to simulate the loading process in a simple way, we imposed a descending velocity to the particles at the top of the cylinder and an ascending one to the particles at the bottom.

It is very important to choose a proper value for the velocity because the result obtained varies significantly from one value to another.

Thereby, we had to impose a velocity that was high enough to perform the experiment in a reasonable time, but not too much, because a very fast loading process would need a very low time step to avoid distortions of the results and so the calculation time would increase considerably. That being said, we chose a velocity of 0,0625 m/s after various attempts.

Furthermore, some of the particles with descending or ascending imposed velocity were fixed in the other two directions so that the specimen was immobile.

In the following figure we have coloured the particles of the test tube with prescribed velocity.

Fig. 60. Particles with imposed velocities in the UCS test.

Prescribed Velocity of coloured particles			
Colour	V_x (m/s)	V_y (m/s)	V_z (m/s)
	Not fixed	-0,0625	Not fixed
	0,0	-0,0625	0,0
	0,0	0,0625	0,0
	Not fixed	0,0625	Not fixed

Table 10. Values of the imposed velocities in the UCS test.

After that, the experiment was ready to be performed.

Post-processing and analysis of results

We wanted to draw the stress – strain graph of the test so that we could obtain the compressive strength of the specimen and its Young's modulus.

The stress at every time step is computed as the quotient between the applied force and the cross-sectional area of the specimen. However, since we load the specimen by imposing descending and ascending velocities, we do not know the applied force. Therefore, we consider the force that a compression plate would apply during the test as the sum of the vertical component of the spring forces acting on each one of the particles with prescribed velocity at the top of the test tube.

Thereby, at every time step, we compute the stress as:

$$\text{Stress} = \frac{\text{Applied Force}}{\text{Cross Sectional Area}} = \frac{\sum_{i=1}^{n} F_{svi}}{\pi r_s^2} \qquad \text{(Eq. 46)}$$

Where F_{svi} are the vertical components of the spring forces acting on the n particles with prescribed velocity at the top of the test tube, and r_s is the radius of the specimen, in this case, 7,5 cm.

To calculate the strain, on the other hand, we simply took into account that the deformation at a time step m is the product of the imposed velocity at both extremes of the specimen and the total elapsed time:

$$\text{Strain}_m = \frac{2 \cdot \text{Descending Velocity} \cdot \sum_{j=1}^{m} \Delta t}{\text{Height of the Specimen}} \qquad \text{(Eq. 47)}$$

In the end, we obtained the following graph:

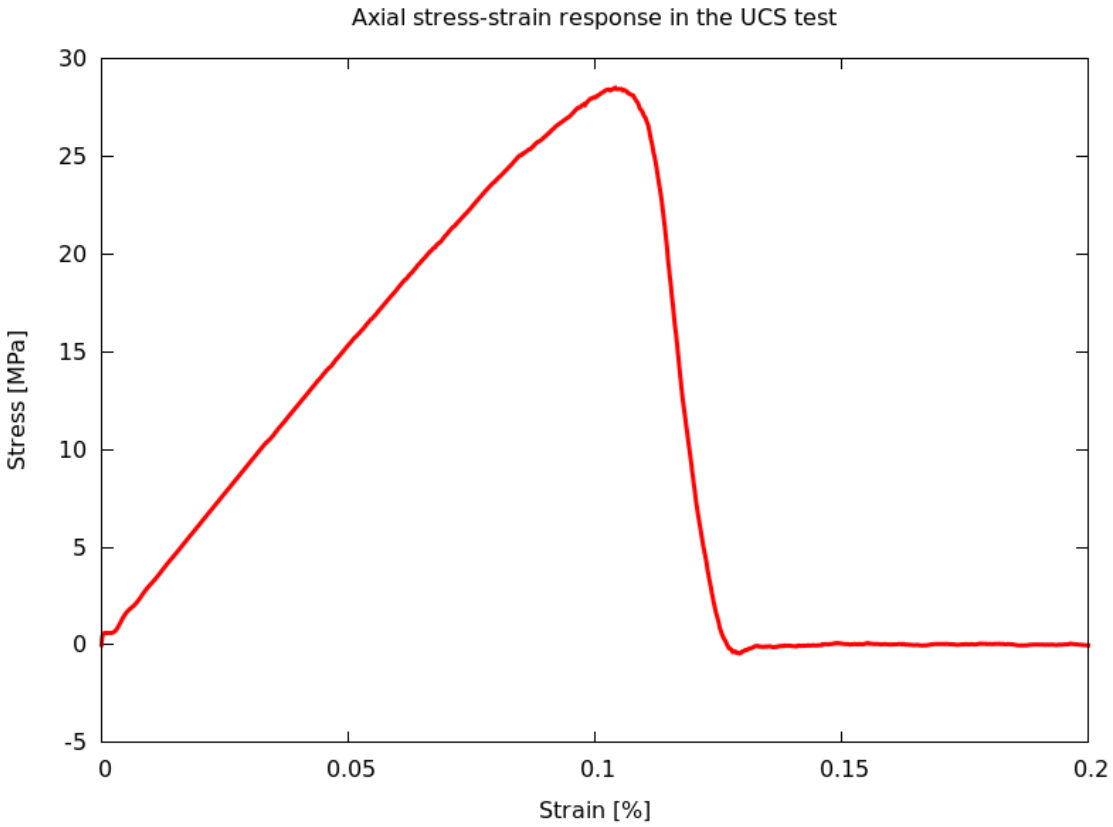

Fig. 61. Stress - strain response in the UCS test.

As a result of the linear-spring-dashpot model of the DEM application, the stress grows linearly with the strain until the accumulation of broken contacts leads to the failure of the specimen. We can see that this failure propagates quickly and after very little deformation. Therefore, as it is been stated before, the failure criterion reproduces a brittle fracture.

The maximum compressive stress obtained is around 28,5 MPa. Furthermore, we can obtain the experimental Young's modulus of the test tube by measuring the

slope of the graph.

$$E = \frac{\sigma}{\varepsilon} \simeq 28 \text{ GPa}$$

We can compute now the relative error of the experimental results by comparing it with the theoretical values of the UPC specimen.

$$r_{fck} = \frac{32{,}8 - 28{,}5}{32{,}8} = 0{,}131 = 13{,}1\ \%$$

$$r_E = \frac{|24 - 28|}{24} = 0{,}167 = 16{,}7\ \%$$

Although the experimental results are not bad, they are still considerably different from the theoretical ones. In order to get better results, we could either change the failure parameters, or modify the general approach of the failure criterion so as to represent more properly the behaviour of the material.

In order to show the failure in a more visual way we represented the contacts between neighbouring particles as coloured bars.

In red we show the contacts that have already failed. At the end of the experiment, one can see large diagonal cracks:

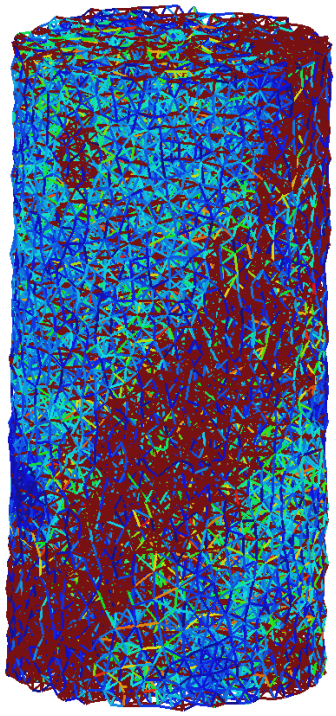

Fig. 62. Fracture of contacts after the UCS test.

We can see more clearly how the specimen fails with the deformed mesh x5 at the end of the test. As we can see, the DEM allows us to obtain impressive fractures.

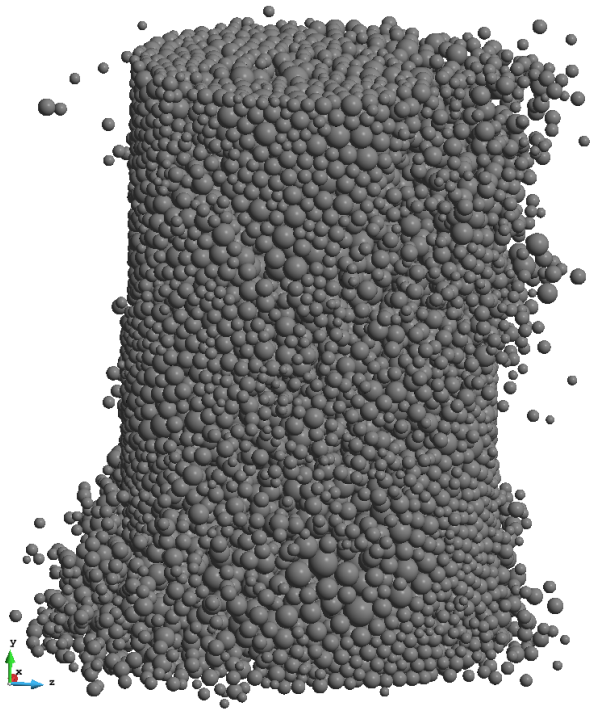

Fig. 63. Deformed mesh x5 after the UCS test.

7.2.2. Indirect Tensile Strength Test

7.2.2.1. Introduction

The Indirect Tensile Strength Test or Brazilian Test performs the case of a cylindrical test tube loaded with a diametric compression along two opposed generatrices. This load configuration causes uniform tensile forces on the diametric loading plane that bring about the failure of the test tube along this vertical plane.

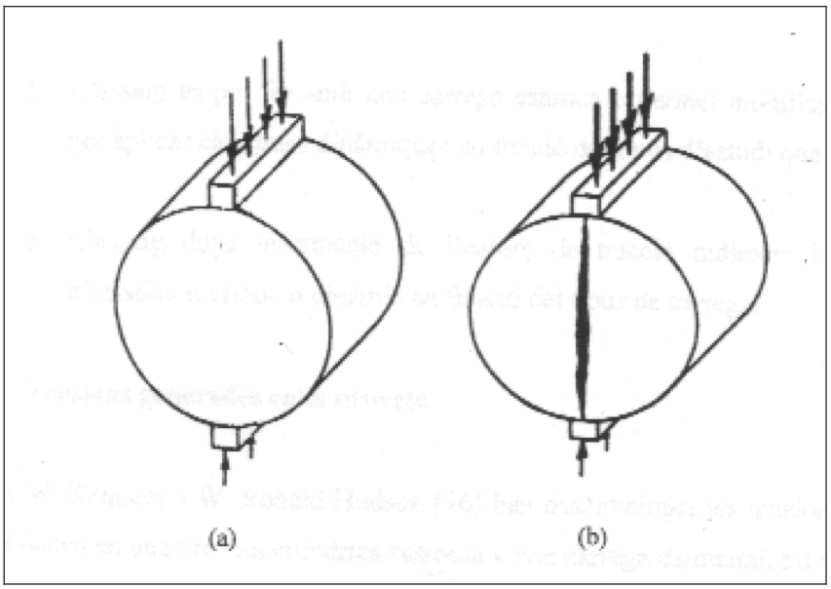

Fig. 64. Scheme of the loading process in a Brazilian test.

Tomas W.Kennedy and W.Ronald Hudson studied the theoretical stresses that appear in a cylindrical test tube under a diametric load. The distribution of these stresses is showed in the following figure:

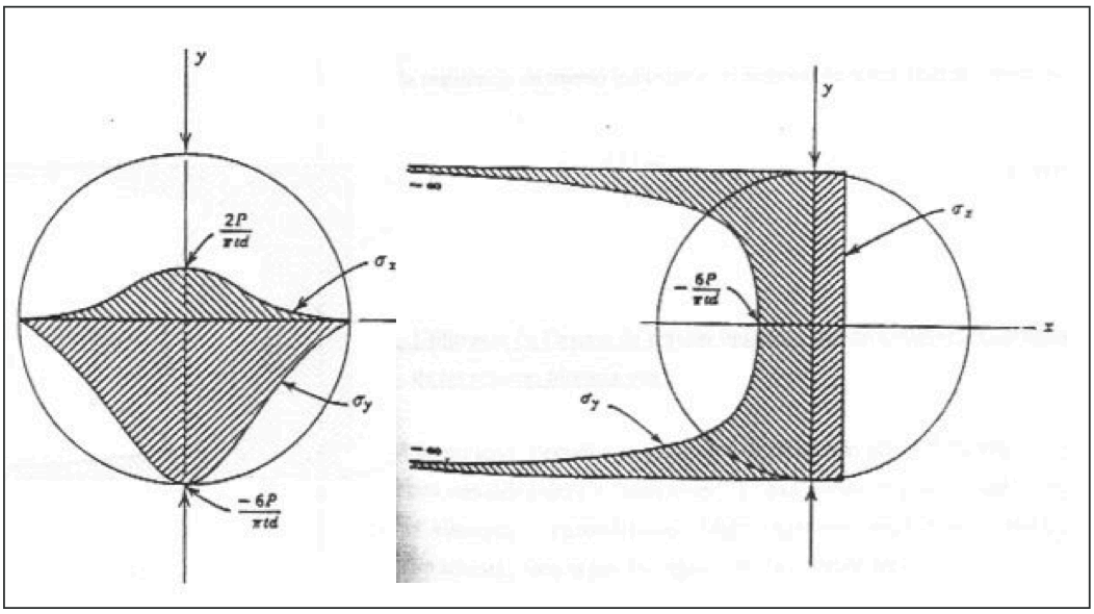

Fig. 65. Distribution of stresses in a Brazilian test.

The aim of the experiment is the measurement of the tensile strength of the material, and to do so, we need to measure the ultimate force applied on the test tube.

Let P_{max} be the ultimate force, t the height of the test tube and d the diameter. The tensile strength S_t is computed as follows:

$$S_t = \frac{2 \cdot P_{max}}{\pi \cdot t \cdot d} \qquad \text{(Eq. 48)}$$

7.2.2.2. DEM simulation

The goal of this test is to break a concrete specimen under a diametric compression in order to calculate its tensile strength.

To assess this experimental result, we can estimate the expected tensile strength from the compression strength with the following formula extracted from the EHE-08:

$$\text{Expected tensile strength} = 0{,}3 \cdot f_{ck}^{(2/3)} \qquad \text{(Eq. 49)}$$

Since we are using the same concrete that in the uniaxial compression strength test, we have f_{ck} = 32,8 MPa. Therefore:

Expected tensile strength = $0{,}3 \cdot 32{,}8^{(2/3)}$ = 3,07 MPa

Pre-processing

I started sketching a cylindrical test tube with a diameter of 15 cm and a height of 7,5 cm.

In this case, instead of prescribing a velocity to some of the particles of the specimen, we decided to add external rows of particles with imposed velocity that would simulate the loading process. The blue lines surrounding the specimen in the figure below are the basis of the additional rows of particles.

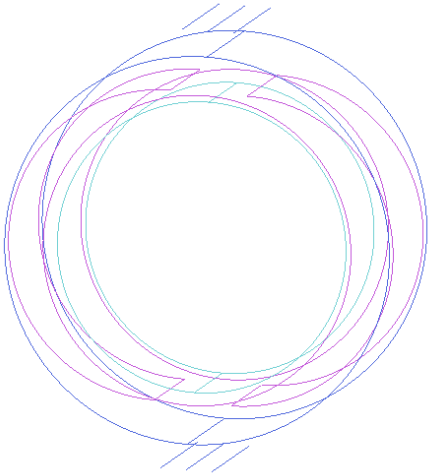

Fig. 66. Geometry of the specimen for a Brazilian test.

Once again, we defined the properties of the material and the characteristics of the experiment.

Material	
Particle Density	2.500 [Kg/m^3]
Young's Modulus	24 [GPa]
Poisson Ratio	0,2
Dynamic Friction Angle	40 º
Restitution Coefficient	0,0
Problem Data	
DEM simulation	Continuum
Integration Scheme	Forward Euler
Search Step	150
Time Step	$9 \cdot 10^{-8}$ [s]
Simulation Time	0,003 [s]
Failure criterion	Uncoupled
τ_{tmax}	8,5 [MPa]
σ_{tmax}	3,3 [MPa] [6]
Internal Friction Angle, ϕ	26,6°

Table 11. Characteristics of the Brazilian test.

[6] Remember that this is the value of the maximum tensile stress applied at the contacts in the particulate level. It is not necessarily the same as the tensile strength of the specimen we are trying to model.

Afterwards, we meshed the cylinder with a non-uniform distribution of approximately 7.600 spheres. The lines used to load the specimen were filled with identical particles of 1 cm of radius.

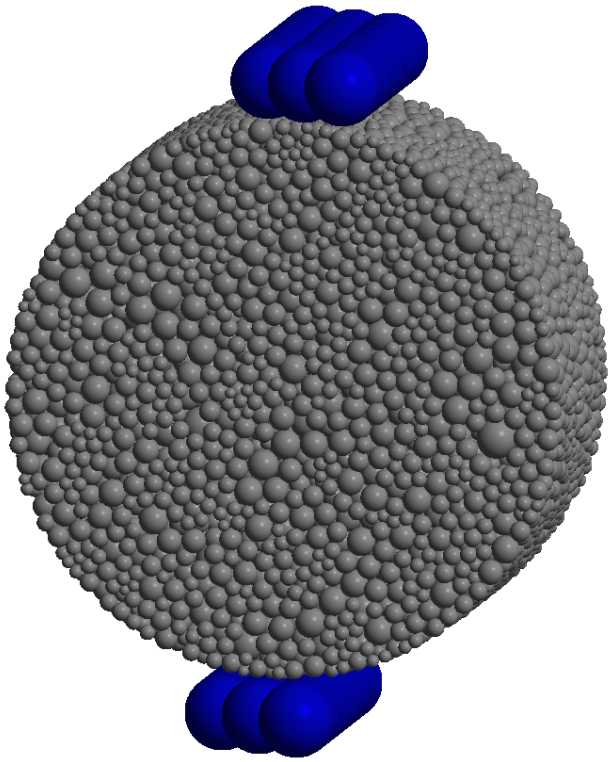

Fig. 67. Mesh of the specimen for a Brazilian test.

After that, we imposed a descending velocity to the upper rows of particles and an ascending one to the lower rows. In this test, we chose a velocity of 0,05 m/s.

Fig. 68. Particles with imposed velocity in a Brazilian test.

Prescribed Velocity of coloured particles			
Colour	V_x (m/s)	V_y (m/s)	V_z (m/s)
	0,0	0,0	-0,05
	0,0	0,0	0,05

Table 12. Values of the prescribed velocity in the Brazilian test.

Post-processing and analysis of results

We have represented the force – displacement graph of the experiment because, as it has been stated in the introduction of this test, we need to obtain the ultimate force applied on the test tube in order to compute its tensile strength.

Just like in the previous test, the applied force is computed as the sum of the vertical component of the spring forces acting on each particle of the upper rows.

On the other hand, the displacement at time step m is obtained from:

$$\text{displacement}_m = 2 \cdot \text{descending velocity} \cdot \sum_{j=1}^{m} \Delta t \qquad \text{(Eq. 50)}$$

Finally, the resulting graph is the following:

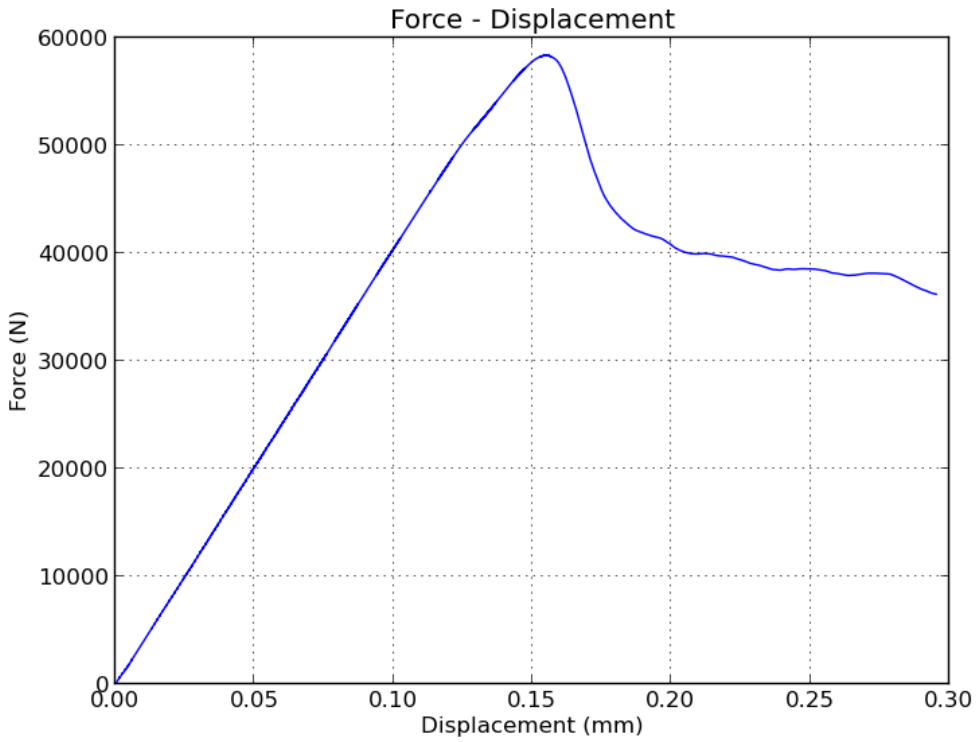

Fig. 69. Force – displacement relation in the Brazilian test.

As we can see, there is a linear relation between the displacement and the force applied in the first half of the graph. After the critical point is reached, the graph starts falling quickly, but then the specimen maintains some residuary force.

Thereby, the ultimate force obtained is over 58.500 N. By substituting this value in the previous formula, we can calculate the tensile strength:

$$S_t = \frac{2 \cdot 58.500}{\pi \cdot 75 \cdot 150} = 3{,}31 \text{ MPa}$$

Although the value of the tensile strength obtained is practically the same that the maximum tensile stress set for this test, we should not generalize this result, since after various attempts we cannot guarantee such a simple relation.

Once again we can compare the result obtained with the theoretical one by computing the relative error:

$$r_{St} = \frac{|3{,}07 - 3{,}31|}{3{,}07} = 0{,}078 = 7{,}8\ \%$$

Like before, we show in red the contacts that have already failed. At the end of the experiment we observe a concentration of cracks at the zone of application of the load, and an important diametric crack:

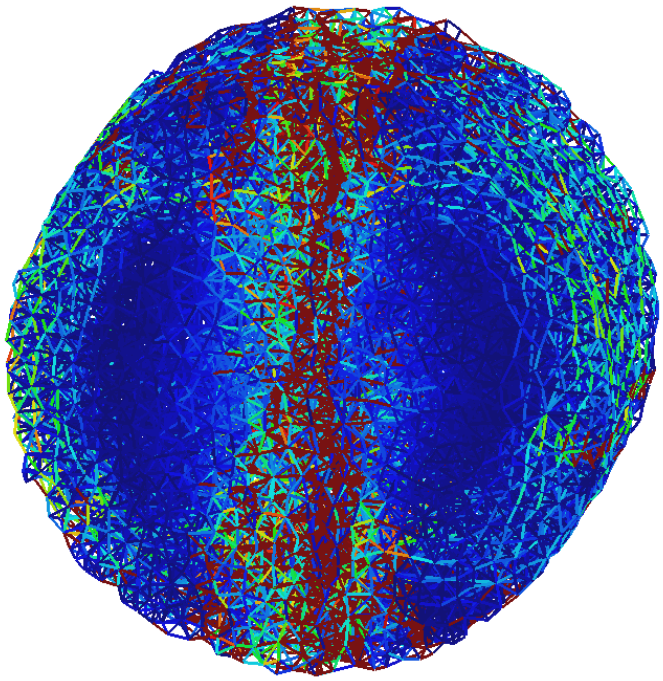

Fig. 70. Fracture of contacts after the Brazilian test.

The deformed mesh x5 at the end of the test represents what we have already seen with the failed contacts.

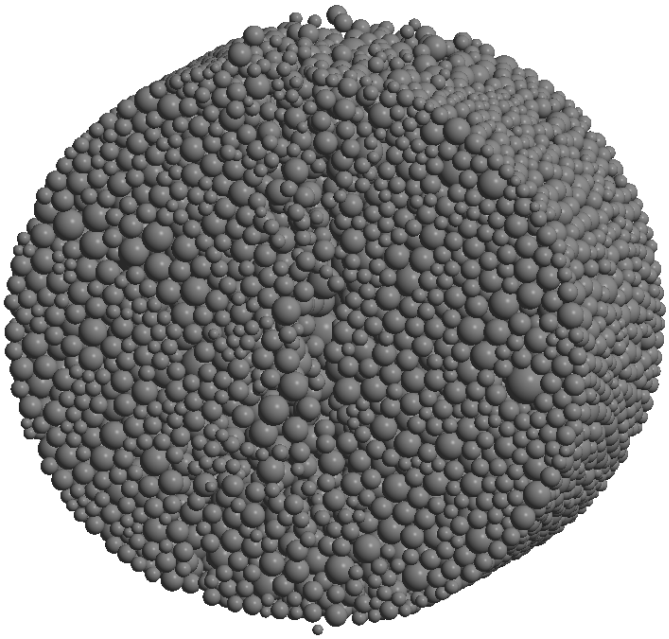

Fig. 71. Deformed mesh x5 after the Brazilian test.

In order to see more clearly the final response of the elements, the horizontal displacement of the particles at the end of the experiment is shown in the next picture. As a result of the diametric crack, half of the spheres are moving to the right (in red) and half of them to the left (in blue).

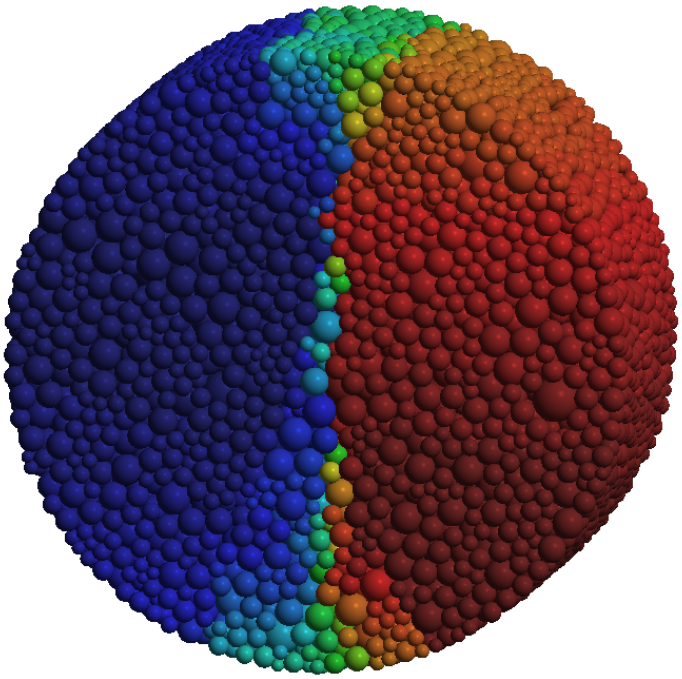

Fig. 72. Horizontal displacements after the Brazilian test.

7.2.3. Triaxial Compression Strength Test

7.2.3.1. Introduction

The behaviour of concrete under high levels of confinement is of significant importance in several engineering problems, such as the design of the anchorage of pre-stressing reinforcement, containment vessels, bridge piles and columns of high-rise buildings.

The testing of concrete under triaxial stresses can provide valuable information, not only for design purposes but also for the development and validation of constitutive models.

A cylindrical specimen is stressed under conditions of axial symmetry in the manner shown in figure.

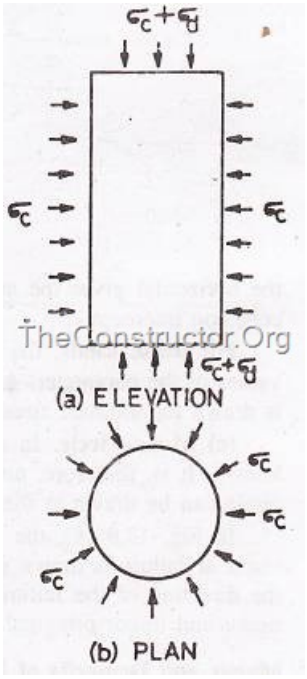

Fig. 73. Load case in a triaxial test.

The specimen is subjected to an all round fluid pressure in the cell, consolidation is allowed to take place if appropriate, and then the axial stress is gradually increased by the application of compressive load through the ram until failure of the specimen takes place, usually on a diagonal plane.

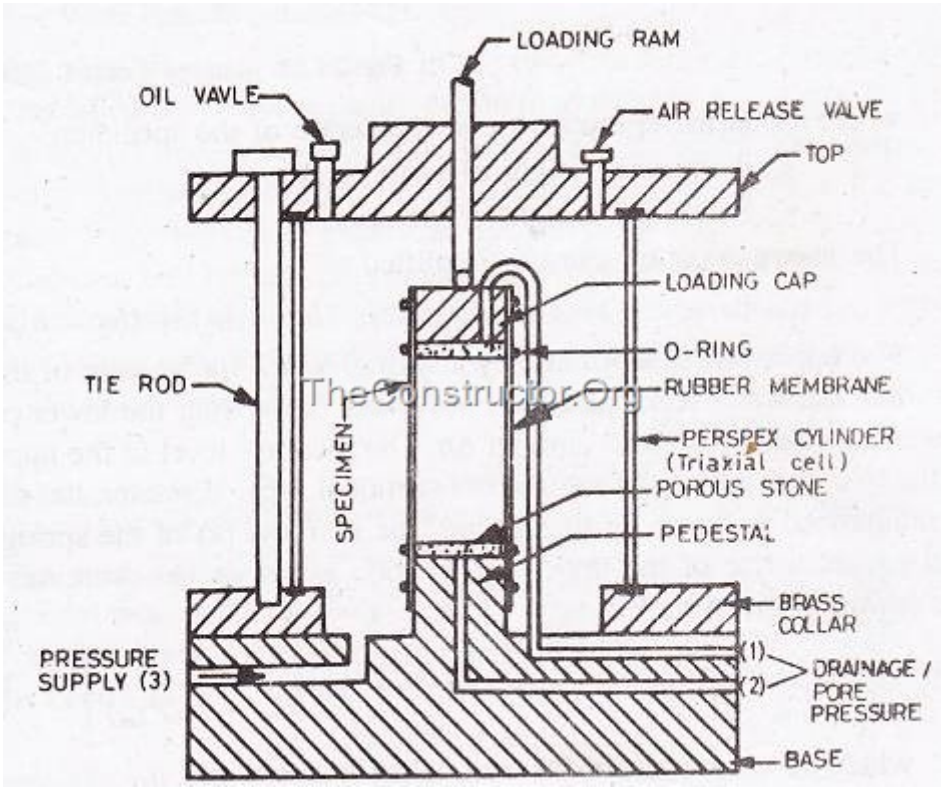

Fig. 74. Triaxial test apparatus.

7.2.3.2. DEM simulation

The purpose of this last test is to break various concrete specimens under a triaxial compression load in order to compare their axial stress-strain responses at different confining pressures with laboratory results of other researchers [2].

The DEM simulation starts with the confinement of the specimen. The pressure is obtained through the application of confining forces to the spheres of the boundary. The sum of all these individual forces divided by the surface area of the test tube must equal the predefined pressure. After this pressure is reached the specimen is loaded axially until failure like in the uniaxial compression strength test.

These tests are carried out with the same confining pressures and concrete that in the laboratory experiments, i.e. we have performed six tests with confining pressures of 1,5 MPa, 4,5 MPa, 9 MPa, 30 MPa, 60 MPa, and the concrete with no pressure has a compressive strength of 32,8 MPa and a Young's modulus of 27,3 GPa.

Pre-processing

Since the specimen used in this test is the same that the one used in the UCS test, we have reused the mesh and so this pre-processing is virtually the same.

The only differences are in the material properties and problem data.

Material	
Particle Density	2.500 [Kg/m^3]
Young's Modulus	27,3 [GPa]
Poisson Ratio	0,2
Dynamic Friction Angle	40 º
Restitution Coefficient	0,0
Problem Data	
DEM simulation	Continuum
Integration Scheme	Forward Euler
Search Step	150
Time Step	$5 \cdot 10^{-8}$ [s]
Simulation Time	0,05 [s]
Failure criterion	Uncoupled
τ_{tmax}	8,5 [MPa]
σ_{tmax}	3,3 [MPa]
Internal Friction Angle, ϕ	26,6 °

Table 13. Characteristics of the triaxial test.

Just like in the uniaxial compression strength test, in order to simulate the loading process in a simple way, we imposed a velocity of -0,0625 m/s to the particles at the top of the cylinder and a velocity of 0,0625 m/s to the particles at the bottom. Again, some of the particles with descending or ascending imposed velocity were fixed in the other two directions so that the specimen was immobile.

Before running the tests, the desired confining pressure must be predefined by the user in the characteristics of the problem.

Post-processing and analysis of results

In order to compare the results of the triaxial test performed with DEM with those of the experiments carried out in laboratory, we have represented the axial stress-strain responses for all the tests.

The graphs of the DEM simulations have been obtained just as it has been explained for the UCS test.

If we first look at the laboratory results:

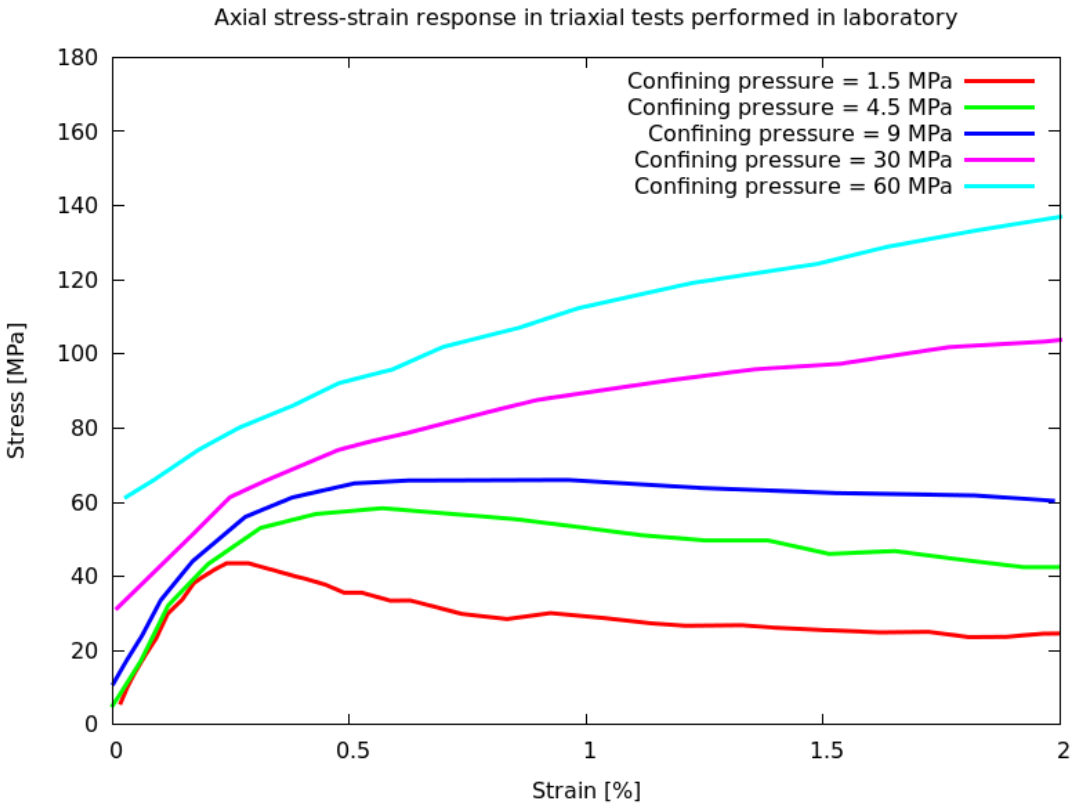

Fig. 75. Stress – strain response in triaxial tests performed in laboratory.

And now the same tests performed with DEM:

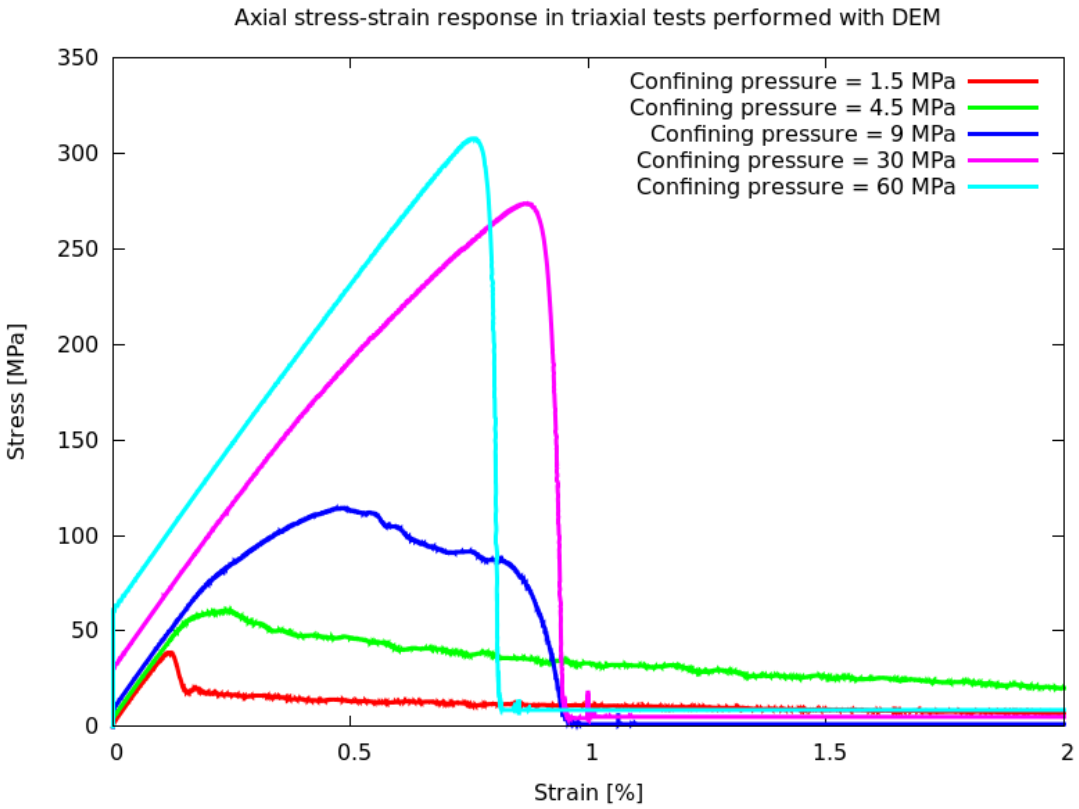

Fig. 76. Stress – strain response in triaxial tests performed with DEM.

It is easy to see that they are quite different. However, let us check each test one by one:

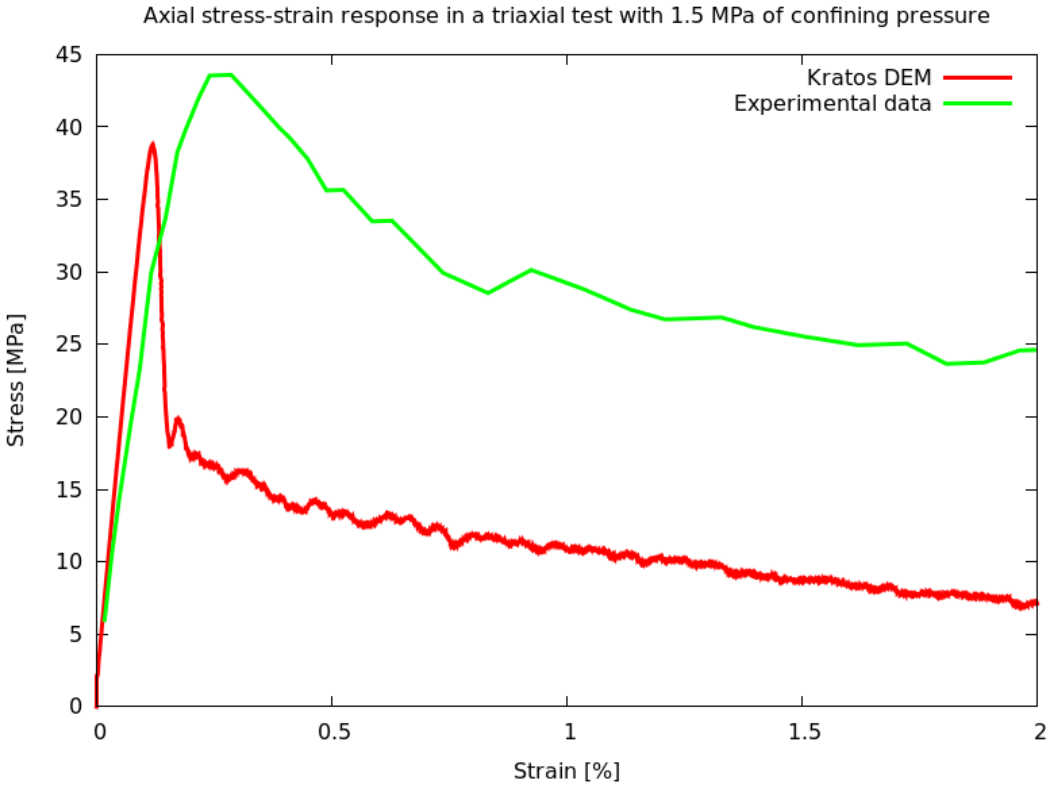

Fig. 77. Stress – strain response in a triaxial test with a pressure of 1,5 MPa.

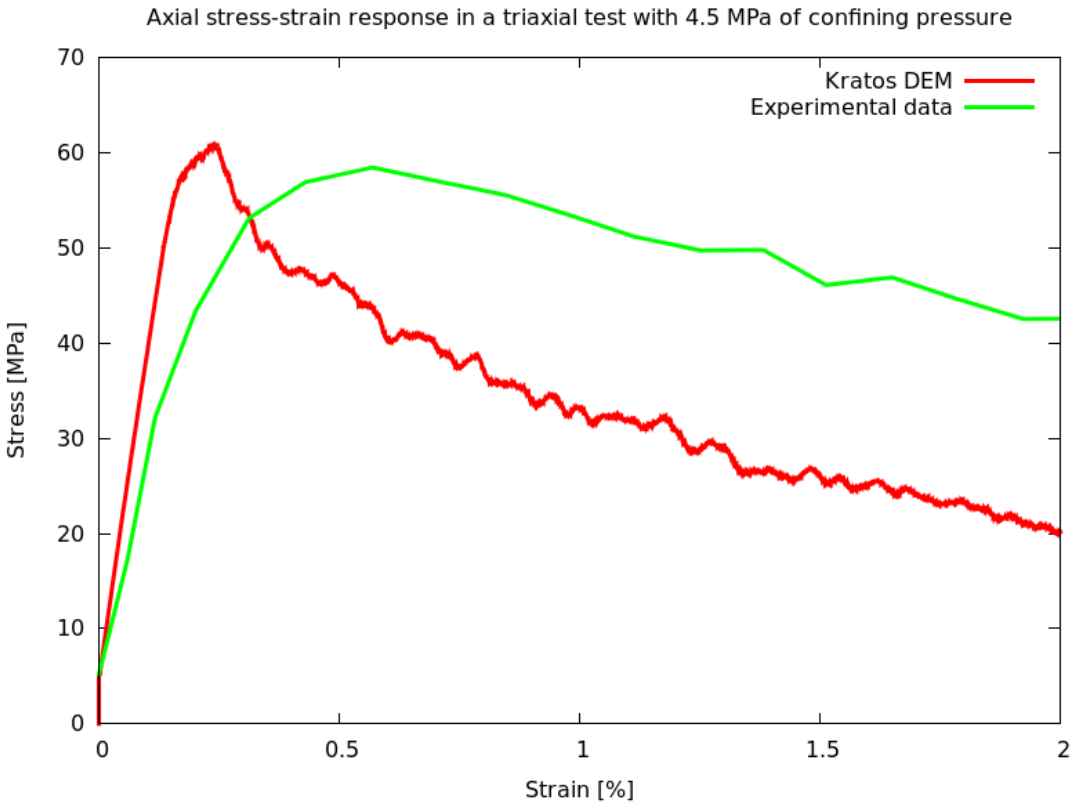

Fig. 78. Stress – strain response in a triaxial test with a pressure of 4,5 MPa.

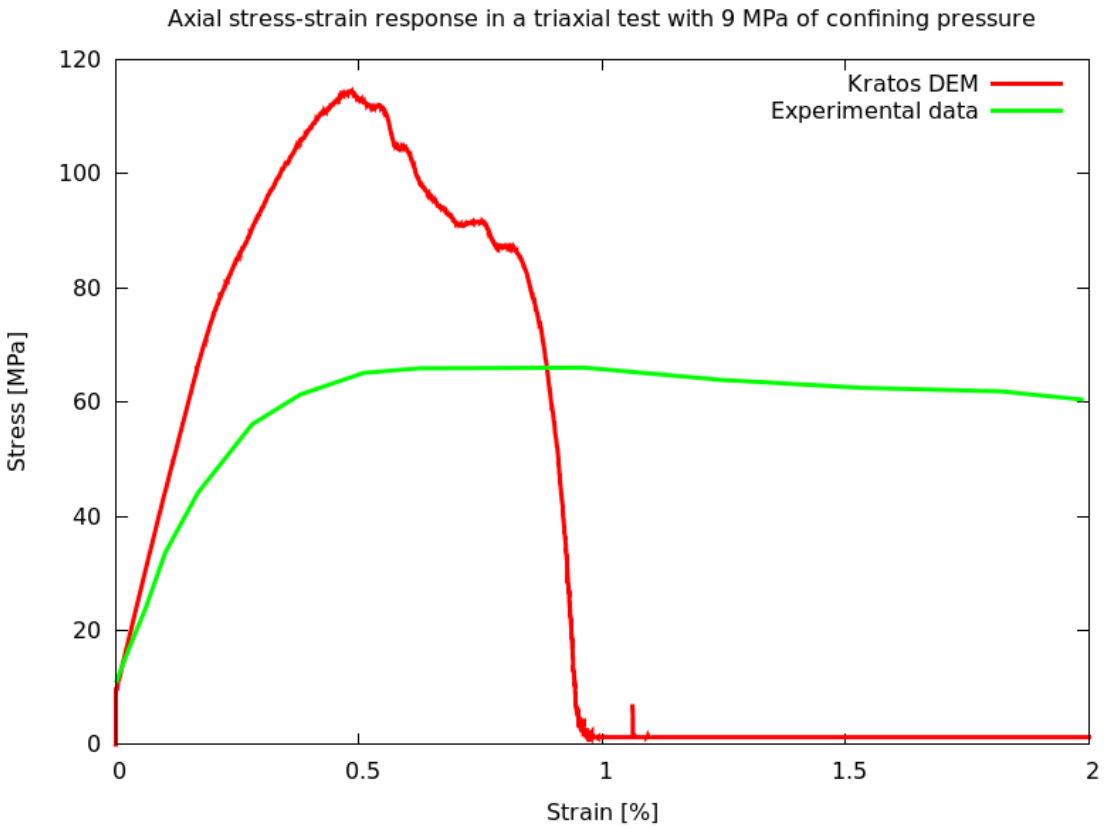

Fig. 79. Stress – strain response in a triaxial test with a pressure of 9 MPa.

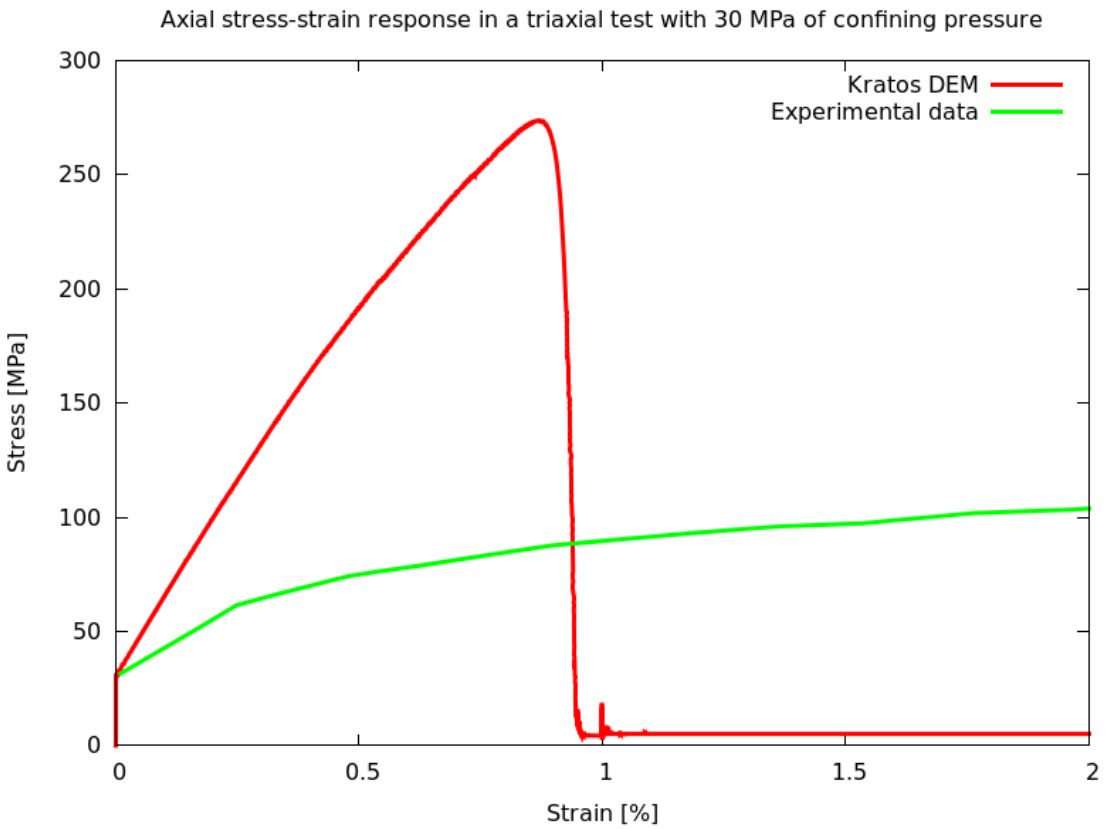

Fig. 80. Stress – strain response in a triaxial test with a pressure of 30 MPa.

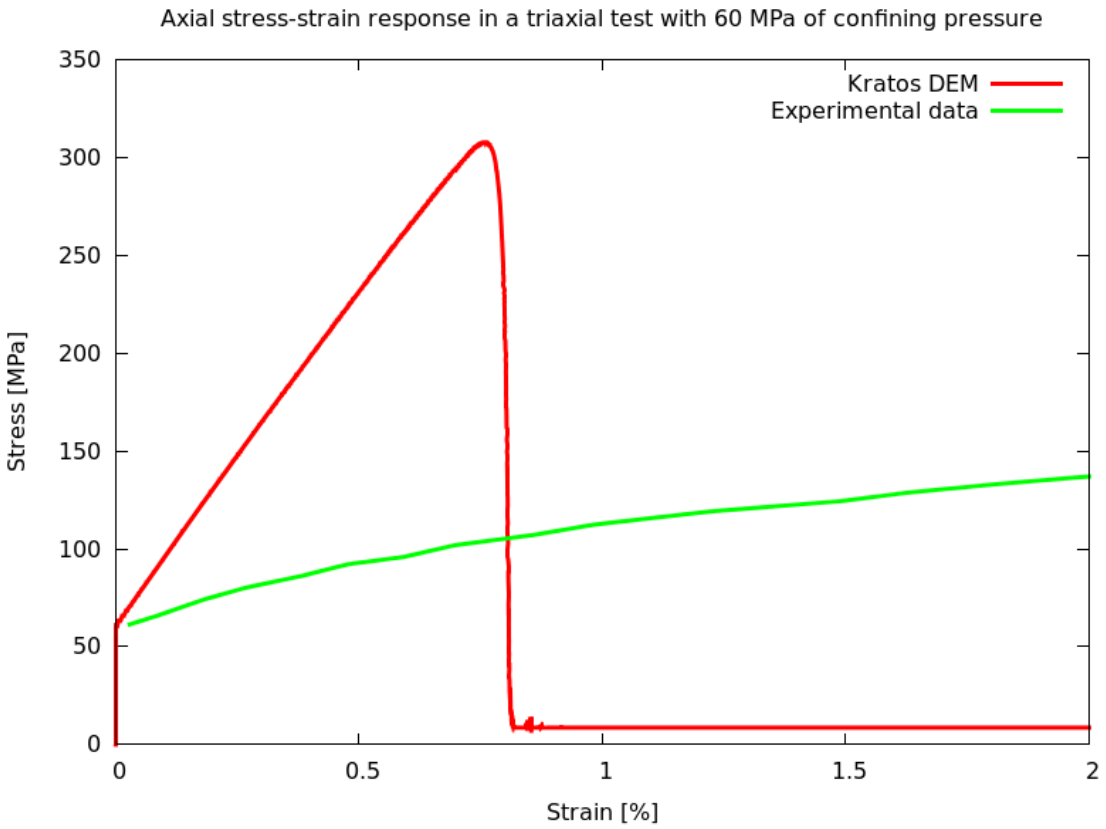

Fig. 81. Stress – strain response in a triaxial test with a pressure of 60 MPa.

As one can see, these results obtained with DEM are simply not good. Although for confining pressures of 1,5 MPa and 4,5 MPa the responses are somehow alike, in the other tests they are utterly different and the reason is quite clear from the graphs. The response of the concrete simulated with DEM is too stiff and brittle.

As I have commented in the paragraphs of *Brittle-ductile fracture*, the failure criterion applied in the tests can only reproduce brittle fracture, and does not take into account the elastoplastic behaviour of concrete. As a result, the slope of the graph is too high and the specimen fails "without warning".

In order to obtain a better result, we should introduce damage and plasticity models that could represent properly the fracture.

For the moment, we have managed to introduce a kind of elastoplastic response just by modifying the stiffness of the contacts after a certain stress is reached. It is a simple method in which we consider a piecewise linear behaviour for concrete, and the results of which depend basically on the calibration of the implied parameters.

Since this is still under research, in this work I will only show some final results, with the mentioned modification, without going into details.

For instance, by using this modification of stiffness, the triaxial tests with 9 MPa and 30 MPa of confining pressure show the following graphs:

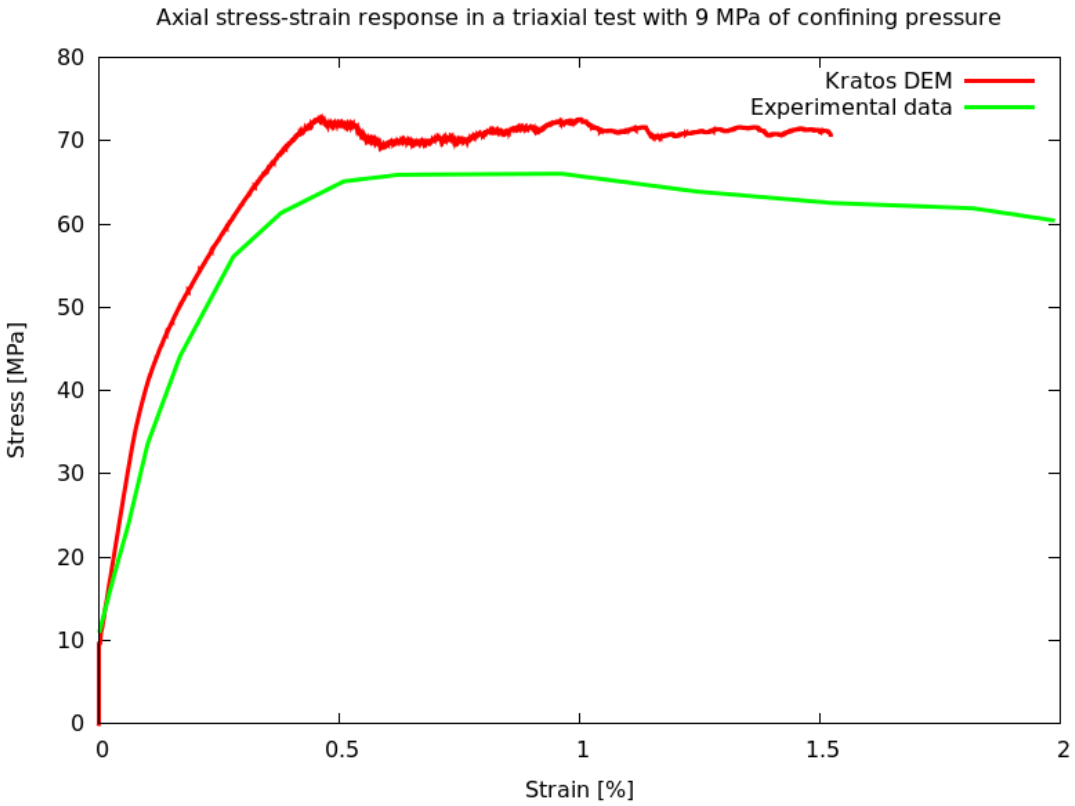

Fig. 82. Improved stress – strain response with a pressure of 9 MPa.

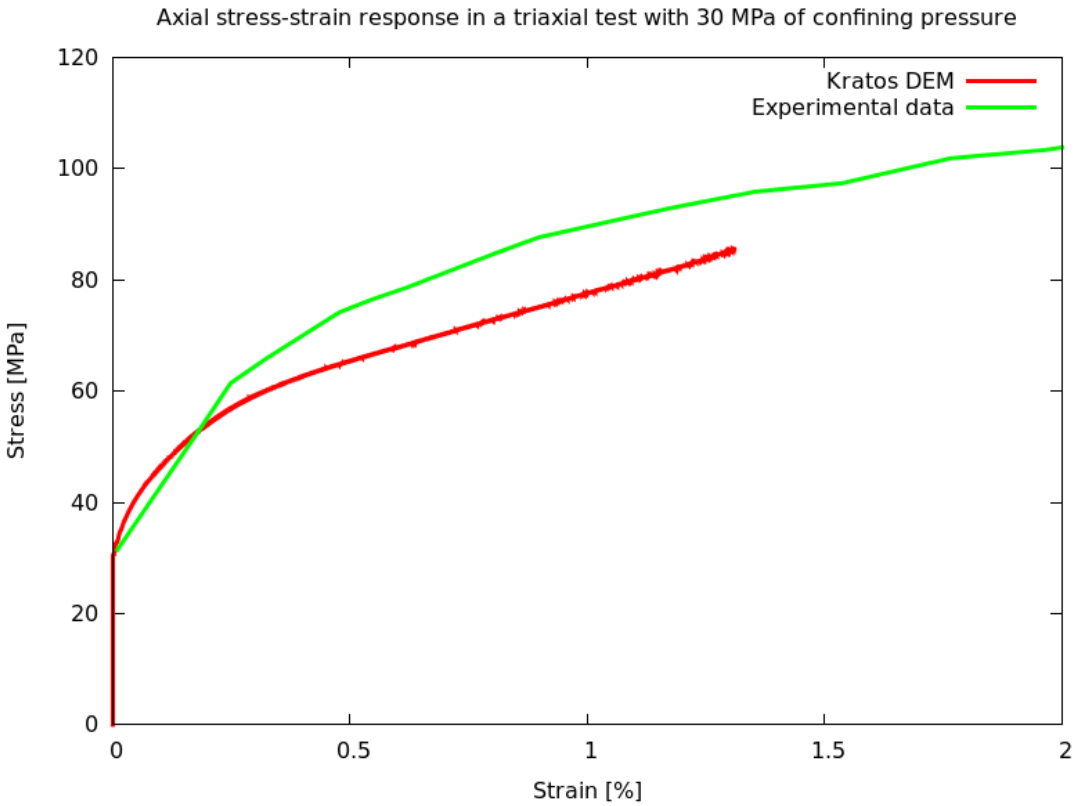

Fig. 83. Improved stress – strain response with a pressure of 30 MPa.

As we can observe, the responds obtained now fit the experimental data much

better than before and so, although more research is needed, this may be an effective method when the parameters are properly calibrated.

8. Present and future research lines of DEM Application

In this work we have seen that the DEM application can already be used to simulate some discontinuum and continuum cases with quite good results in various cases. However, it has still a long way to go until it can show all its potential in a range of branches.

To begin with, in this work we have only been using spherical particles. Nonetheless, as I have already stated before, there are other kinds of particles, such as polyhedra and ellipses, which could be used to emulate more accurately stones and other granular material in discontinuum simulations. These alternative shapes are much more complicated to implement than the spherical particles. In the case of hexahedra, for instance, one should take into account interaction between face and face, face and edge, face and vertex, edge and edge, edge and vertex, and vertex and vertex for the search of neighbours and computation of forces.

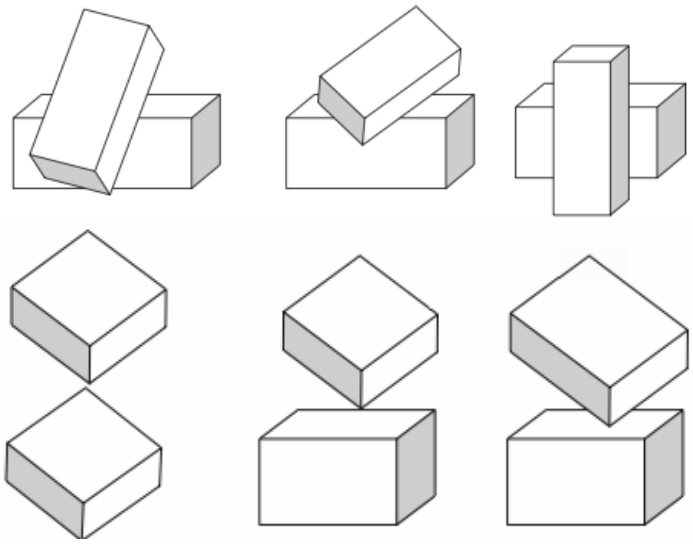

Fig. 84. Possible interactions between hexahedral elements.

Apart from that, flow of fluids and interaction between fluids and solids are other areas in which the Discrete Element Method could play an important role. Although more research needs to be done, one could analyse problems related to sand and wind in beaches, river flow, magnetic fields, etc.

With regard to continuum, we must notice that the Discrete Element Method was not originally developed to simulate it. DEM is computationally more costly than other approaches that have proved to work nicely in this kind of problems, e.g. the Finite Element Method, and it could seem unnecessary to apply it for continuum. However, it is generally agreed that DEM has a great potential to find multi-fracture in solids because of its granular nature, and so it may actually be useful in continuum simulations. Therefore, there is still space for the innovation in this subject, and in CIMNE we have already thought of the first steps to follow:

- Improve the computation of elastic deformations and Poisson effect

- Calculate the stress tensor for every particle
- Define properly a yield surface
- Introduce a good post-critic behaviour, implementing plasticity, damage or coupling both of them, in order to reproduce ductile fracture

Another field of study is the combination of the Discrete Element Method and the Finite Element Method (DEM-FEM) to approach a range of problems:

- Interaction between FEM-discretized bodies and DEM-discretized domains

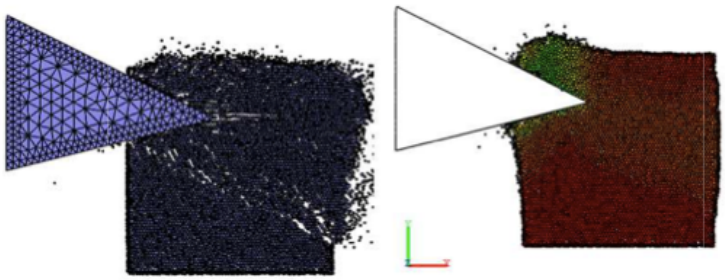

Fig. 85. Interaction FEM - DEM.

- Creation of DEM particles from fractured FEM elements

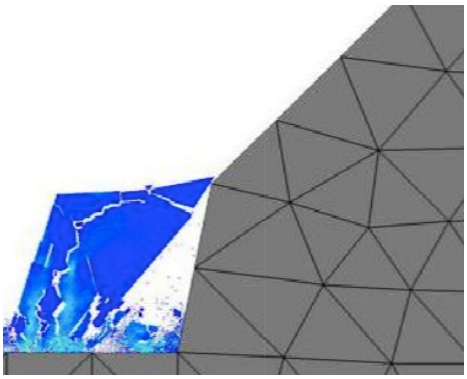

Fig. 86. Fracture of FEM.

- FEM discretization of DEM particles

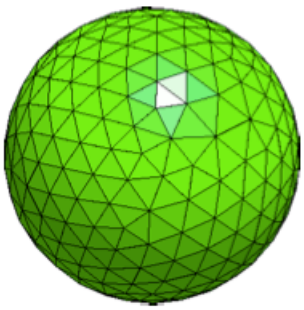

Fig. 87. FEM discretization of a DEM sphere.

- DEM discretization of FEM elements

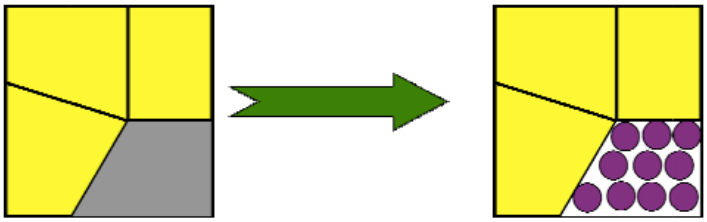

Fig. 88. DEM discretization of a FEM quadrilateral.

One last subject that must be considered is parallelization. As it has been commented before, a Discrete Element Method code without parallelization is limited in practice.

There exist two kinds of remarkable architectures for computers, the Shared Memory Machines (SMM), and the Distributed Memory Machines (DMM). While SMM offer a single memory space used by all processors, in DMM each processor has its own private memory.

There are two typical techniques of parallelization suitable for C++ language: Open Multiprocessing (Open MP), and Message Passing Interface (MPI). Open MP works fine with SMM and makes each CPU compute a different part of a loop. On the other hand, MPI works properly with DMM and divides the total number of iterations of the loops among various CPUs.

Most of the tests of this work have been performed using Open MP parallelization. Furthermore, MPI is currently being used by other researchers and has already been tested with 64 processors with a good speed up.

9. Conclusions

After a whole year working with the Discrete Element Method I can say that it has proven to be a great numerical technique to model the behaviour of granular and particulate systems. The fundamentals are quite simple, but the results are visually impressive, as we have seen in the sand clock model. Probably the most limiting characteristic is the computational cost of the method, although developers are already working in this sense to reduce the total calculation time.

Continuum simulations, on the other hand, are clearly much more complicated to deal with. With regard to DEM application, we have been able to model some cases with reasonable good results, but it has still a long way to go until it can be actually competitive against other methods such as the Finite Element Method.

From the continuum experiments performed in this work we can say that DEM Application shows a quite good response in the elastic range of the problems, but fails to model properly the elastoplastic behaviour of materials like concrete. Furthermore, the Application only reproduces brittle fracture and lacks a more global failure criterion that should include plasticity models and damage, as well as the conservation of the fracture energy of the material.

Nonetheless, due to its particulate nature, the method has the potential to be an effective tool to model problems that are characterized by a transformation from a continuum to a discontinuum, such as failure of concrete structures, fragmentation of rock due to blasting, and fracture of ceramics and other quasi-brittle materials under high velocity impact.

As a final comment, I think that more research needs to be done and some changes in the interface could be introduced to make the DEM Application more user-friendly, but I do believe that this application can become a really powerful help for engineers when solving a range of different problems.

10. References

[1] Kevin Francis, M., Bao Hua, X., 2008. Determination of contact parameters for discrete element method simulations of granular systems. Particuology 6 (6), 521-528. http://dx.doi.org/10.1016/j.partic.2008.07.012.

[2] Sfer, D., Carol, I., M.ASCE, Gettu, R., Etse, G., 2002. Study of the behaviour of concrete under triaxial compression. Journal of Engineering Mechanics 128 (2), 156-163. http://dx.doi.org/10.1061/(ASCE)0733-9399(2002)128:2(156)

[3] Hedjazi, L., Martin, C.L., Guessasma, S., Della Valle, G., Dendievel, R., 2012. Application of the Discrete Element Method to crack propagation and crack branching in a vitreous dense biopolymer material. International Journal of Solids and Structures 49 (13), 1893-1899. http://dx.doi.org/10.1016/j.ijsolstr.2012.03.030.

[4] Tavarez, F.A., Plesha, M.E., 2006. Discrete element method for modelling solid and particulate materials. International Journal for Numerical Methods in Engineering 70, 379-404. DOI: 10.1002/nme.1881.

[5] André, D., Iordanoff, I., Charles, J., Néauport, J., 2012. Discrete element method to simulate continuous material by using the cohesive beam model. Computer Methods in Applied Mechanics and Engineering 213-216, 113-125. http://dx.doi.org/10.1016/j.cma.2011.12.002.

[6] Mishra, B.K., Rajamani, Raj K., 1992. The discrete element method for the simulation of ball mills. Applied Mathematical Modelling 16 (11), 598-604. http://dx.doi.org/10.1016/0307-904X(92)90035-2

[7] Cundall, P.A., L–Strack, O.D., 1979. A discrete numerical model for granular assemblies. Geotechnique 29 (1), 47-65.

[8] Cundall, P.A., 1971. A computer model for simulating progressive, large-scale movements in blockly rock systems, in Symposium Soc. Internat Mécanique des Roches: Nancy, 2-8.

[9] Pande, G., Beer, G., Williams, J.R., 1990. Numerical Modeling in Rock Mechanics. John Wiley and Sons.

[10] Munjiza, A., 2004. The combined Finite-Discrete Element Method. John Wiley & Sons.

[11] Santasusana Isach, Miquel. Continuum modelling using the Discrete Element Method. Theory and implementation in a object-oriented software platform. Tesina d'Enginyeria de Camins Canals i Ports, UPC. 2012. [UPCommons]

[12] Oliver, Xavier, Argelet, Carlos, 2000. Mecánica De Medios Continuos Para Ingenieros. Edicions UPC. Universitat Politècnica de Catalunya. Barcelona.

[13] Durán, O., Kruyt, N., Luding, S., 2010. Analysis of three-dimensional micro-mechanical strain formulations for granular materials: evaluation of accuracy. International Journal of Solids and Structures 47 (2), 251–260. http://dx.doi.org/10.1016/ j.ijsolstr.2009.09.035.

[14] Bonelli, S., Millet, O., Nicot, F., Rahmoun, J., De Saxcé, G., 2012. On the definition of an average strain tensor for two-dimensional granular material assemblies. International Journal of Solids and Structures 49 (7-8), 947-958. http://dx.doi.org/10.1016/j.ijsolstr.2011.11.005.

[15] Li, X., Yu, H.S., Li, X.S., 2009. Macro‐micro relations in granular mechanics. International Journal of Solids and Structures 46 (25-26), 4331-4341. http://dx.doi.org/10.1016/j.ijsolstr.2009.08.018.

11. List of figures

12. List of tables